

The Delay Time Distribution of Tidal Disruption Flares

Nicholas C. Stone^{*1}, Aleksey Generozov¹, Eugene Vasiliev^{2,3}, Brian D. Metzger¹

¹*Columbia Astrophysics Laboratory, Columbia University, New York, NY, 10027, USA*

²*Rudolf Peierls Centre for Theoretical Physics, Oxford, OX1 3NP, UK*

³*Lebedev Physical Institute, Moscow, 119991, Russia*

^{*}*Einstein Fellow; nstone@phys.columbia.edu*

Received / Accepted

ABSTRACT

Recent observations suggest that stellar tidal disruption events (TDE) are strongly overrepresented in rare, post-starburst galaxies. Several dynamical mechanisms have been proposed to elevate their TDE rates, ranging from central stellar overdensities to the presence of supermassive black hole (SMBH) binaries. Another such mechanism, introduced here, is a radial velocity anisotropy in the nuclear star cluster produced during the starburst, which temporarily enhances the stellar flux into the loss cone of a solitary SMBH. These, and other, dynamical hypotheses can be disentangled by comparing observations to theoretical predictions for the TDE *delay time distribution* (DTD). We show that SMBH binaries are a less plausible solution for the post-starburst preference, as they predict an unrealistically top-heavy distribution of primary SMBH masses, and can only reproduce the observed DTD with extensive fine-tuning. The overdensity hypothesis produces a reasonable match to the observed DTD (based on the limited data currently available), provided that the initial stellar density profile created during the starburst, $\rho(r)$, is exceptional in both steepness and normalization. In particular, explaining the post-starburst preference requires $\rho \propto r^{-\gamma}$ with $\gamma \gtrsim 2.5$, i.e. much steeper than the classic Bahcall-Wolf equilibrium profile of $\gamma = 7/4$. For “ultrasteep” density cusps ($\gamma \geq 9/4$), we show that the TDE rate decays with time measured since the starburst as $\dot{N} \propto t^{-(4\gamma-9)/(2\gamma-3)} / \ln t$. Radial anisotropies also represent a promising explanation, provided that initial anisotropy parameters of $\beta_0 \approx 0.5$ are sustainable against the radial orbit instability. TDE rates in initially anisotropic cusps will decay roughly as $\dot{N} \propto t^{-\beta_0}$. As the sample of TDEs with well-studied host galaxies grows, the DTD will become a powerful tool for constraining the exceptional dynamical properties of post-starburst galactic nuclei.

1 INTRODUCTION

Stellar tidal disruption events (TDEs) have long been seen as powerful tools for studying the demography of quiescent supermassive black holes (SMBHs). The death of a star during a strong tidal encounter with an SMBH (Hills 1975) is expected to produce a luminous, multiwavelength flare (Rees 1988). Many such flares have now been detected through thermal emission in optical (van Velzen et al. 2011; Gezari et al. 2012; Chornock et al. 2014; Holoien et al. 2014; Blagorodnova et al. 2017; Hung et al. 2017), ultraviolet (Gezari et al. 2006, 2008), and soft X-ray (see e.g. Komossa 2015; Auchettl et al. 2017) wavelengths, while others have been seen through nonthermal emission in the radio (Zauderer et al. 2011; van Velzen et al. 2016) or hard X-ray (Bloom et al. 2011; Cenko et al. 2012; Brown et al. 2015). The observed sample of TDEs is expected to grow from dozens to thousands in the near future (van Velzen et al. 2011; Khabibullin et al. 2014). This large future sample carries great promise for studying SMBH demography, although there are many open theoretical questions that must be resolved before TDE light curves can be translated into SMBH mass (Lodato et al. 2009; Guillochon & Ramirez-Ruiz 2013; Hayasaki et al. 2013; Piran et al. 2015) or spin (Stone & Loeb 2012; Hayasaki et al. 2016; Franchini et al. 2016) measurements.

While the prospects for using TDE light curves to study

SMBH demography lie in the future, the statistical properties of our current TDE sample *have already* revealed unexpected dynamical processes in distant galactic nuclei. Arcavi et al. (2014) were the first to notice the peculiar host galaxy preference of observed optically-selected TDEs: in the Palomar Transient Factory sample of three strong TDE candidates, two were found in E+A galaxies, a rare, post-starburst galaxy type that makes up $\approx 0.2\%$ of all galaxies in the low-redshift universe. E+A galaxies exhibit strong H δ absorption features indicative of many young A stars, but little to no H α emission line strength, signaling an absence of ongoing star formation. Subsequent observations of TDE host galaxies also found that an order unity fraction of these flares inhabit this exceedingly uncommon galaxy subtype.

French et al. (2016, 2017) conducted the first thorough statistical examination of TDE host galaxy properties, finding that both classical E+A galaxies and more weakly post-starburst galaxies were strongly overrepresented in their host sample. This second host galaxy subpopulation exhibits a similar dearth of ongoing star formation but weaker H δ absorption features. Its combination of emission and absorption properties is found in $\approx 2\%$ of low redshift galaxies, and is consistent with an older post-starburst galaxy, or alternatively a young post-starburst galaxy that underwent a weaker episode of star formation (French et al. 2017 find some degener-

acy between these two explanations of strong H δ features). In a sample of 8 TDE hosts, classical E+A's and weaker post-starburst galaxies were overrepresented by factors of $\mathcal{R} = 190^{+115}_{-100}$ and $\mathcal{R} = 33^{+7}_{-11}$, respectively. Qualitatively similar results were found by a more recent analysis of a larger sample of optically and X-ray bright tidal disruption flare hosts (Graur et al. 2017), though with a somewhat reduced overrepresentation of post-starburst galaxies among TDE hosts (using the same cuts on H δ absorption strength, the rare host overrepresentation fell to factors of $\mathcal{R} = 36^{+22}_{-18}$ and $\mathcal{R} = 18^{+8}_{-6}$; see also Law-Smith et al. 2017 for complementary analysis). TDE hosts clearly exhibit a strong post-starburst preference (PSP), though the exact magnitude of this preference remains an area of active research.

This finding is even more puzzling when juxtaposed against a broader TDE rate discrepancy (Stone & Metzger 2016): observational estimates, although limited by small sample sizes and selection effects that are difficult to quantify, often find per-galaxy TDE rates $\dot{N} \sim 1 - 2 \times 10^{-5} \text{ gal}^{-1} \text{ yr}^{-1}$ (Donley et al. 2002; van Velzen & Farrar 2014). These are at least an order of magnitude below conservative theoretical estimates for TDE rates (set by two-body relaxation) in realistic galactic nuclei, which are typically $\dot{N} \gtrsim 10^{-4} \text{ gal}^{-1} \text{ yr}^{-1}$ (Wang & Merritt 2004; Stone & Metzger 2016), although we note that some observed TDE samples find rates up to $\dot{N} \sim 1 - 2 \times 10^{-4} \text{ gal}^{-1} \text{ yr}^{-1}$ (Esquej et al. 2008; Holoien et al. 2016). Although dynamical mechanisms to suppress TDE rates have been proposed, they seem unlikely to work in practice (Lezhnin & Vasiliev 2015, 2016). The resolution of this rate discrepancy (which is worsened by the PSP) may be a very broad TDE luminosity function (e.g. Blagorodnova et al. 2017), of which we have so far only seen the bright end. Indeed, recent modeling of the optical TDE luminosity function suggests an observational rate $\dot{N} \approx 1 \times 10^{-4} \text{ gal}^{-1} \text{ yr}^{-1}$ (van Velzen 2017). The broader rate discrepancy is not yet a solved problem, but in this paper we make the reasonable assumption that the TDE luminosity function is the same in post-starburst and normal galaxies, and search for dynamical explanations for the PSP¹.

What dynamical mechanisms could be elevating the TDE rate so dramatically following a starburst? Arcavi et al. (2014) proposed that, as many starbursts are triggered by galaxy mergers, the PSP may reflect a population of SMBH binaries (SMBHBs) which, as they harden, pass briefly through a stage where TDE rates are increased by many orders of magnitude. Stone & Metzger (2016) suggested that if the starburst is preferentially concentrated in the galactic nucleus, then a strong stellar overdensity may be formed, which would increase TDE rates by decreasing the two-body relaxation timescale. This overdensity hypothesis has received tentative observational support from observations and dynamical modeling of one of the nearest E+A galaxies, NGC 3156 (Stone & van Velzen 2016); likewise, broader population studies find that per-galaxy TDE rates are correlated with both the slope (Law-Smith et al. 2017) and the normalization (Graur et al. 2017) of stellar light profiles on $\sim \text{kpc}$ scales (though we caution that the TDE rate is set by stellar dynamics on $\sim \text{pc}$ scales). Other possibilities exist as well: rates could be enhanced due to non-conservation of orbital angular momentum in a triaxial potential created by starburst

¹ Non-dynamical effects - e.g. preferential nuclear obscuration in normal galaxies, that is absent in post-starburst galaxies - could contribute to both the PSP and the overall TDE rate discrepancy, but in this paper we focus on dynamical hypotheses for intrinsically elevated rates of disruption in post-starburst galaxies.

or galaxy merger (Magorrian & Tremaine 1999; Merritt & Poon 2004), or due to secular dynamics in eccentric nuclear stellar disks (Madigan et al. 2017).

We propose that the several extant hypotheses for the PSP, as well as many more yet to be suggested by theorists, can be disentangled by empirical construction of a TDE *delay time distribution* (DTD). Different dynamical mechanisms for enhancing TDE rates in a starburst will attenuate over time, as the galaxy ages and its nuclear properties evolve to resemble those of more typical galaxies. But different dynamical solutions to the PSP will make different predictions for exactly how TDE rates decline with time since the starburst, and these predictions can be tested against observations. The results of French et al. (2016), French et al. (2017), and Graur et al. (2017) represent the first empirical TDE DTDs, although they are limited by small number statistics. In the near future, the *Zwicky Transient Facility* (ZTF) and *Large Synoptic Survey Telescope* (LSST) will discover tens to thousands of TDEs per year, respectively, and empirical DTDs may definitively test theoretical explanations for the PSP.

In this paper, we estimate rates and, when possible, DTDs for three different dynamical hypotheses that aim to explain the post-starburst preference. In §2, we review the basis for the overdensity hypothesis and make simple estimates for the time evolution of TDE rates in overdense galactic nuclei. In §3, we introduce a new dynamical explanation for the PSP, one predicated on velocity-space anisotropies biased toward radial orbits; we also estimate the time evolution of TDE rates in this scenario. In §4, we review the SMBHB hypothesis and, again, estimate how quickly an elevated TDE rate decays against time since starburst. In §5 we combine our analysis of the prior three scenarios and make a first comparison to the observed DTD of tidal flares, and in §6 we summarize this work and offer thoughts on its future extensions.

2 OVERDENSE STELLAR SYSTEMS

Empirically, the starbursts that create E+A galaxies preferentially concentrate star formation in their central regions. Spectroscopic observations of E+A's find strong radial color gradients, indicating that the youngest stars are concentrated in the galactic nucleus (Pracy et al. 2012, 2013), though the resolution of these studies has historically been insufficient to provide detailed information on the SMBH influence radius. Given the overrepresentation of nuclear regions in the star formation history of post-starburst galaxies, it is natural to speculate that central overdensities are responsible for the PSP: overdense galactic nuclei will possess short two-body relaxation times, and the rapid diffusion of stars through orbital phase space will result in a high rate of stellar tidal disruption.

Some support for this hypothesis was found by Stone & van Velzen (2016), who analyzed archival *Hubble Space Telescope* (*HST*) photometry of the nearby E+A galaxy NGC 3156, and found an unusually steep stellar density cusp which should produce an elevated TDE rate ($\dot{N} \approx 1 \times 10^{-3} \text{ gal}^{-1} \text{ yr}^{-1}$) due to rapid two-body relaxation. However, the small sample size of this study means that confirmation of the overdensity hypothesis will need to wait for future *HST* observations of other nearby post-starburst galaxies.

Enhanced TDE rates due to central stellar overdensities will decline over time, as two-body relaxation diffuses stars onto wider orbits, or as the dense stellar population drains into the SMBH. To quantify this decline, it is useful to consider how two-body relaxation diffuses stars into the SMBH loss cone (LC), the region of stellar phase space where specific orbital angular momentum J is

less than a critical value $J_{\text{LC}} = \sqrt{2GM_{\bullet}R_t}$. Here we have defined the tidal radius $R_t \equiv R_{\star}(M_{\bullet}/M_{\star})^{1/3}$ as the radius interior to which a star of mass M_{\star} and radius R_{\star} will be torn apart by tides from a black hole of mass M_{\bullet} . Near the SMBH, per-orbit perturbations (from two-body relaxation, or other processes) to specific angular momentum ΔJ are weak, with $\Delta J/J_{\text{LC}} \ll 1$; here the LC is devoid of stars and the rate of stellar tidal disruption is the rate at which stars diffuse into it. Far from the SMBH, $\Delta J/J_{\text{LC}} \gg 1$ and the LC is full; the per-star TDE rate here is, crudely, the fractional size of the LC in angular momentum space divided by a stellar orbital period. The transition between these two regimes occurs at the critical radius r_{crit} where $\Delta J = J_{\text{LC}}$ (Merritt 2013).

For spherically symmetrical galactic nuclei, time-dependent TDE rates can be found by numerically integrating the 2D (energy and angular momentum) Fokker-Planck equation (Cohn & Kulsrud 1978), and quasi-steady state rates can be derived in a more semi-analytic way (Magorrian & Tremaine 1999; Wang & Merritt 2004). We review some results from the quasi-steady state LC formalism in Appendix A, but the basic picture is as follows. Starting from a 3D stellar mass density profile $\rho(r)$ and gravitational potential $\psi(r)$, we compute the stellar distribution function (DF) $f(\epsilon, J)$. In general this is a two-integral DF, written in terms of J and specific energy² ϵ , but if velocities are isotropic it simplifies to $f(\epsilon)$. Using the DF, one finds orbit-averaged diffusion coefficients $\bar{\mu}(\epsilon)$ for the radial orbits of interest, and from these one can calculate the flux of stars into the LC, $\mathcal{F}(\epsilon)$. The total TDE rate is $\dot{N} = \int \mathcal{F}(\epsilon) d\epsilon$. We will first perform this exercise for a fully analytic toy model of $\rho(r)$ and $f(\epsilon)$, and then repeat the procedure using time-dependent numerical solutions to the 1D (energy) Fokker-Planck equation.

2.1 Analytic Evolution of Stellar Overdensities

Consider an idealized spherical profile of stars: $\rho(r) = \rho_{\text{infl}}(r/r_{\text{infl}})^{-\gamma}$, where the SMBH influence radius r_{infl} is defined as the radius that encloses the SMBH's own mass in stars, so $\rho_{\text{infl}} = M_{\bullet}(3 - \gamma)/(4\pi r_{\text{infl}}^3)$. For simplicity we will assume an isotropic distribution of velocities (but see §3 for the more general anisotropic case); this yields a stellar DF $f(\epsilon) \propto \epsilon^{\gamma-3/2}$. In this model, there are two qualitatively different locations from which the bulk of the LC flux originates. In typical, relatively shallow density cusps ($\gamma < 9/4$), most of the LC flux comes from radii $r \approx r_{\text{crit}}$. However, in much steeper density cusps ($\gamma > 9/4$), the LC flux actually *diverges* at small radii (Syer & Ulmer 1999); in reality, this indicates that the single power law assumption is not self-consistent, and most of the tidal disruptions will be sourced from whatever small radius corresponds to a break in the larger scale power law density profile. For the remainder of this paper, we refer to $\rho(r)$ profiles with $\gamma > 9/4$ as “ultrasteep.” One can imagine two ways in which centrally concentrated star formation could provide an elevated TDE rate:

- The formation of an ultrasteep cusp in a galactic nucleus with a relatively normal value of r_{infl} .
- The formation of a very dense stellar cusp with a more typical slope γ but an atypically small value of r_{infl} . We refer to such a cusp as “overconcentrated.”

Because stars are typically fed into the LC from the influence radius or smaller scales, both of these scenarios are compatible with

² In this paper we adopt the stellar dynamics convention where bound orbits have $\epsilon > 0$.

starbursts that only increase the total galactic bulge mass by small amounts (see e.g. the burst mass fractions estimated among TDE hosts in French et al. 2017). The latter scenario (low r_{infl}) would require an order unity or greater increase in stellar mass within the pre-starburst influence radius, while the former (large γ) scenario requires even less total star formation. These two possibilities are not mutually exclusive.

Almost all observed galactic nuclei possess $\gamma < 9/4$ (Lauer et al. 2005), but Stone & van Velzen (2016) found that the nucleus of NGC 3156, a nearby E+A galaxy, is at the very least a borderline case and may indeed be ultrasteep; depending on the precise model employed for the point spread function of *HST*, this galaxy has $2.15 \leq \gamma \leq 2.31^3$. If we assume that most of the central stars formed impulsively in a starburst, these (and less steep) central density cusps will relax over time towards a steady state configuration. For a single-species stellar present day mass function (PDMF), this is the well known Bahcall-Wolf cusp, with $\gamma = 7/4$ (Bahcall & Wolf 1976). Multi-species PDMFs will exhibit more complicated density profiles (Bahcall & Wolf 1977; Keshet et al. 2009), but we defer an investigation of this to future work.

So long as the starburst forms a density profile with central $\gamma > 3/2$, relaxation times decrease with decreasing radius r , and the profile relaxes towards a Bahcall-Wolf configuration from the inside-out. Because we are interested primarily in the densest galactic nuclei, we limit ourselves to this regime⁴, and approximate a time dependent density profile as the broken power law

$$\rho(r, t) = \begin{cases} \rho_{\text{infl}}(r/r_{\text{infl}})^{-\gamma}, & r > r_{\text{BW}}(t) \\ \rho_{\text{infl}}(r/r_{\text{BW}})^{-7/4}(r_{\text{BW}}/r_{\text{infl}})^{-\gamma}, & r \leq r_{\text{BW}}(t), \end{cases} \quad (1)$$

where we have defined a “Bahcall-Wolf radius” r_{BW} as the location where the post-starburst age t equals the local energy relaxation time (Stone & van Velzen 2016). In the Keplerian potential of the SMBH, the relaxation time is

$$t_r(r) = \frac{\sigma^2(r)}{\langle \Delta(v_{\parallel})^2 \rangle} = \frac{k(\gamma)(GM_{\bullet})^{3/2} \langle m_{\star} \rangle}{G^2 \langle m_{\star}^2 \rangle \rho_{\text{infl}} r_{\text{infl}}^{\gamma} \ln \Lambda} r^{\gamma-3/2} \quad (2)$$

where $\sigma^2(r) = GM_{\bullet}r^{-1}/(1 + \gamma)$ is the one-dimensional velocity dispersion, $\langle (v_{\parallel})^2 \rangle$ is a local diffusion coefficient defined in Appendix A, and the dimensionless constant $k(\gamma) \approx 0.05$ is defined in that appendix. Here $\langle m_{\star} \rangle$ is the first moment of the stellar mass function and $\langle m_{\star}^2 \rangle$ is the second moment. The Bahcall-Wolf radius is thus

$$r_{\text{BW}} = \left(\frac{k(\gamma)M_{\bullet}^{3/2} \langle m_{\star} \rangle}{G^{1/2} \langle m_{\star}^2 \rangle \rho_{\text{infl}} r_{\text{infl}}^{\gamma} t \ln \Lambda} \right)^{\frac{1}{3/2-\gamma}}, \quad (3)$$

where we have used the Coulomb logarithm $\Lambda \approx 0.4M_{\bullet}/\langle m_{\star} \rangle$. An important caveat to this estimate is that in Eq. 2, we have defined the relaxation time in terms of a local diffusion coefficient. Although this is a reasonable approximation in standard galactic nuclei, it is fundamentally nonlocal, orbit-averaged diffusion coefficients which control energy relaxation. In cusps with $\gamma \geq 2$, orbit-averaged diffusion coefficients become strongly nonlocal. While

³ NGC 3156 also possesses an unusually small influence radius, although measuring this quantity requires extrapolating the fitted power law slope beyond the *HST* resolution limit.

⁴ In principle, one could imagine a starburst producing a shallow power law ($\gamma < 3/2$) with an almost discontinuous density jump to a high- but constant-density core. This scenario would be of interest for the overdensity hypothesis, but would not be well approximated by this section, and should also be considered in future work.

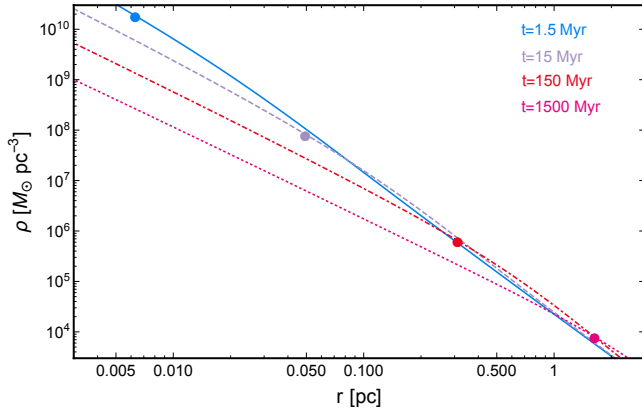


Figure 1. Time evolution of an initially ultrasteep $\rho \propto r^{-2.75}$ stellar cusp using the PHASEFLOW code. The blue solid, purple dashed, red dot-dashed, and pink dotted curves correspond to post-starburst ages $t = 1.5$ Myr, $t = 15$ Myr, $t = 150$ Myr, and $t = 1500$ Myr, respectively. Here we consider a cusp of equal-mass ($M_\star = 1 M_\odot$) stars around a $M_\bullet = 10^6 M_\odot$ SMBH. We mark the Bahcall-Wolf radius r_{BW} with a square on each snapshot in the top panel.

the basic timescale argument behind Eq. 3 remains correct, the simulations of §2.2 allow us to calibrate a fitting formula that better matches Eq. 3 to numerical results: $k(\gamma) \approx 0.045(3 - \gamma)$.

In this toy model, we can apply standard LC theory to extract the time dependent TDE rate \dot{N} (and therefore the DTD) from the density profile given by Eq. 1. In the ultrasteep regime, the DTD can be approximated in closed form using an analytic expression for LC flux $\mathcal{F}(\epsilon)$ from stars deep inside the influence radius of the SMBH (Stone & Metzger 2016, Appendix A). In this regime,

$$\dot{N}_\rho(t) \sim \epsilon_{\text{BW}}(t) \mathcal{F}(\epsilon_{\text{BW}}(t)), \quad (4)$$

where $\epsilon_{\text{BW}} \equiv GM_\bullet / (2r_{\text{BW}})$. Using the analytic diffusion coefficients from Appendix A, we find that in the ultrasteep regime ($\gamma > 9/4$),

$$\dot{N}_\rho(t) \propto t^{-(4\gamma-9)/(2\gamma-3)} / \ln t. \quad (5)$$

A potentially important complication to any scenario involving extremely dense stellar systems is the role of direct physical collisions between stars (e.g. Freitag & Benz 2002). In some portions of parameter space, direct collisions could erode an overdense cusp on timescales shorter than the local relaxation time. For cusps consisting of a single species of stars, the per-star collision rate is

$$\dot{N}_{\text{coll}}(r) = \pi \sqrt{3} R_\star^2 \frac{\rho(r)}{M_\star} \sigma(r) \left(1 + \frac{4GM_\star}{3R_\star \sigma^2(r)} \right) \quad (6)$$

Comparing the relaxation time to the characteristic stellar collision time $t_{\text{coll}} = \dot{N}_{\text{coll}}^{-1}$, we find

$$\frac{t_r}{t_{\text{coll}}} = \pi \sqrt{3} (1 + \gamma)^{3/2} k(\gamma) \frac{\sigma^4(r) R_\star^2}{G^2 \langle m_\star \rangle \ln \Lambda} \left(1 + \frac{4GM_\star}{3R_\star \sigma^2(r)} \right). \quad (7)$$

When $t_r/t_{\text{coll}} \geq 1$, collisional erosion of the stellar cusp dominates relaxational evolution and standard LC theory will strongly overestimate TDE rates. In general, however, $t_r/t_{\text{coll}} \gtrsim 1$ only on very small scales, of $r \lesssim 3 \times 10^{-3}$ pc ($r \lesssim 3 \times 10^{-2}$ pc) for $M_\bullet = 10^6 M_\odot$ ($M_\bullet = 10^7 M_\odot$). As we shall see in §2.2, these scales are only relevant for extremely early periods of post-starburst evolution.

2.2 Numerical Evolution of Stellar Overdensities

To validate the above analytic prescription, we solve the time dependent, isotropic Fokker-Planck equation in energy space. This

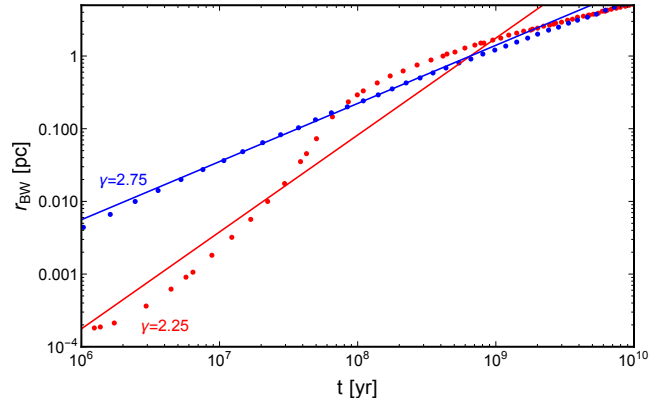


Figure 2. The “Bahcall-Wolf” break radius r_{BW} as a function of time, comparing our numerical calculations (dots) to the analytic approximation in Eq. 3 (solid lines; here we have numerically calibrated the $k(\gamma)$ normalization factor). The time evolution of the numerical Fokker-Planck solutions is well-approximated by our analytic estimate, though the normalization differs by a factor of a few. For the numerical points, this radius is defined as the location where the local logarithmic density slope equals the average of the BW profile’s $\gamma = 7/4$ and the initial power-law slope. Eq. 3 does not perform as well at estimating the time evolution of the marginally ultrasteep $\gamma = 2.25$ initial conditions.

can be written in flux-conserving form as

$$\frac{\partial f(\epsilon, t)}{\partial t} = -\frac{\partial}{\partial \epsilon} \left[D_{\epsilon\epsilon} \frac{\partial f(\epsilon, t)}{\partial \epsilon} + D_\epsilon f(\epsilon, t) \right] - \frac{f(\epsilon, t)}{t_{\text{LC}}(\epsilon, t)}, \quad (8)$$

where D_ϵ and $D_{\epsilon\epsilon}$ are the first and second order diffusion coefficients respectively (see e.g. Merritt 2013). The last term approximates the loss of stars due to angular momentum diffusion into the loss cone for each energy bin (see eq. 13 in Vasiliev 2017, submitted). For a single component system the diffusion coefficients can be written as integrals over the distribution function:

$$D_{\epsilon\epsilon} = 16\pi^2 G^2 m \ln \Lambda \left[h(\epsilon) \int_0^\epsilon f(\epsilon') d\epsilon' + \int_\epsilon^\infty f(\epsilon') h(\epsilon') \right] \quad (9)$$

$$D_\epsilon = -16\pi^2 G^2 m \ln \Lambda \int_\epsilon^\infty f(\epsilon') g(\epsilon') d\epsilon', \quad (10)$$

where $h(\epsilon)$ is the phase volume and $g(\epsilon) = dh(\epsilon)/d\epsilon$ is the density of states.

To solve this equation we use the PHASEFLOW code (Vasiliev 2017).⁵ Our initial conditions, motivated by a rapid burst of star formation, are a power law stellar density profile of $1 M_\odot$ stars with a range of initial power law slopes γ and influence radii $r_{\text{infl},0}$. To avoid divergences in the total mass and stellar potential we introduce an exponential cut-off in the density at 1000 pc and a small r^{-1} core inside of 10^{-4} pc. The inner boundary is absorbing, with the distribution function having a fixed value of zero. The outer boundary condition corresponds to zero flux.

Fig. 1 shows the relaxation of an ultrasteep $r^{-2.75}$ stellar cusp from PHASEFLOW. As expected, the stellar density relaxes to an $r^{-7/4}$ Bahcall-Wolf cusp from the inside-out. In Fig. 2, we plot the evolution of the Bahcall-Wolf transition radius r_{BW} versus time. Eq. 3 captures the time-dependent evolution of the Bahcall-Wolf radius

⁵ PHASEFLOW is part of the AGAMA library for galaxy modelling, available from <https://github.com/GalacticDynamics-Oxford/Agama/>. Note that PHASEFLOW uses the phase volume $h(\epsilon)$ rather than energy as the independent variable.

for $r^{-2.25}$ and $r^{-2.75}$ profiles from $\sim 10^6$ years until r_{BW} approaches the influence radius (because $r_{\text{BW}} \propto t^{1/(\gamma-3/2)}$, the $r^{-2.25}$ profile's break radius deviates from analytic predictions much sooner than does the $r^{-2.75}$ profile's). The agreement between analytic theory and numerical results for the power-law slope of $r_{\text{BW}}(t)$ is quite good in the ultrasteep regime, though the normalization of r_{BW} would differ by a factor of a few between these approaches if we computed $k(\gamma)$ using the local diffusion coefficient of Appendix A. The agreement is worse for shallower profiles. However, the comparison is more ambiguous in this case, as the inner and outer density profiles are similar.

The top panel of Fig. 3 shows the TDE rate as a function of time for different initial density slopes γ . The bottom panel shows how the TDE rate depends on the initial influence radius and compares TDE rates extracted from PHASEFLOW with our analytic approximation (Eq. 4). The analytic prescription reproduces the time evolution of the TDE rate well for the $r^{-2.5}$ and $r^{-2.75}$ profiles. However, the TDE rate from Eq. 4 has a slightly shallower slope at late times than do the numerical results, and the normalization is off by a factor of a few, due to the crudeness of the assumption that $\dot{N}_\rho \sim \epsilon_{\text{BW}} \mathcal{F}(\epsilon_{\text{BW}})$. Eventually, the Bahcall-Wolf radius approaches the initial influence radius $r_{\text{infl},0}$ (the dots on each curve in the top panel of Fig. 3 mark the time when $r_{\text{BW}} = r_{\text{infl},0}$). Afterwards, the evolution of the TDE rate is driven by the expansion of the star cluster due to the consumption of stars, an effect not captured by the analytic model. The analytic prescription is also generally inaccurate for marginally ultrasteep initial density profiles, i.e. $\gamma \approx 2.25$, because for these marginal γ values the LC flux is less sharply peaked at ϵ_{BW} , and the Bahcall-Wolf radius more swiftly overtakes the initial influence radius.

We better quantify the time evolution of the TDE rate by calculating the average power law index for our Fokker-Planck results (i.e. $\dot{N}_\rho \propto t^{-\xi}$, where ξ is averaged between 10^8 yr and 10^{10} yr). The top panel of Fig. 4 shows contours of constant ξ for different values of the initial slope γ of the stellar density profile, and its initial normalization at 1 parsec, $\rho_1(0) \equiv \rho(t=0, r=1 \text{ pc})$. The bottom panel of the same figure shows contours of TDE rate at $t = 100$ Myr in the same parameter space.

Taken together, Figs. 3 and 4 disentangle the loss cone behavior of ultrasteep and overconcentrated cusps. The top panel of Fig. 3 shows strikingly similar rates at post-starburst ages $t \sim 10^8$ yr, implying that - given a constant value of $r_{\text{infl},0}$ - ultrasteep profiles alone are not sufficient to explain the PSP in typical galaxies. In contrast, the bottom panel of Fig. 4 shows that $\dot{N}_\rho(10^8 \text{ yr})$ has a more nontrivial dependence on γ if it is instead $\rho_1(0)$ that is held constant, and the bottom panel of Fig. 3 shows how varying $r_{\text{infl},0}$ into the overconcentrated regime brings post-starburst rates up into agreement with observations. The difference between these two figures highlights how $r_{\text{infl},0}$ becomes a poor metric of overconcentration in the ultrasteep regime. Large changes in initial r_{infl} produce only modest variation in $\rho_1(0)$, and it is the latter that is more predictive of the TDE rate during post-starburst ages $t \gtrsim 10^8$ yr. In most overconcentrated nuclei, the initial influence radius $r_{\text{infl},0}$ expands significantly during 10^{10} yr of relaxational evolution.

In summary, overconcentrated nuclei with low $r_{\text{infl},0}$, or high $\rho_1(0)$, are able to reproduce observed magnitudes of TDE rates in E+A galaxies. Several of the curves in the bottom panels of Figs. 3 and 4 are capable of reproducing the inferred TDE rates in E+A galaxies ($\dot{N} \sim 10^{-3} \text{ yr}^{-1}$; French et al. 2016). In general, increasing the density slope γ increases the initial TDE rate but also increases the steepness of the DTD, while diminishing r_{infl} (or increasing $\rho_1(0)$) increases the early-time TDE rate. The overall slope ξ of the

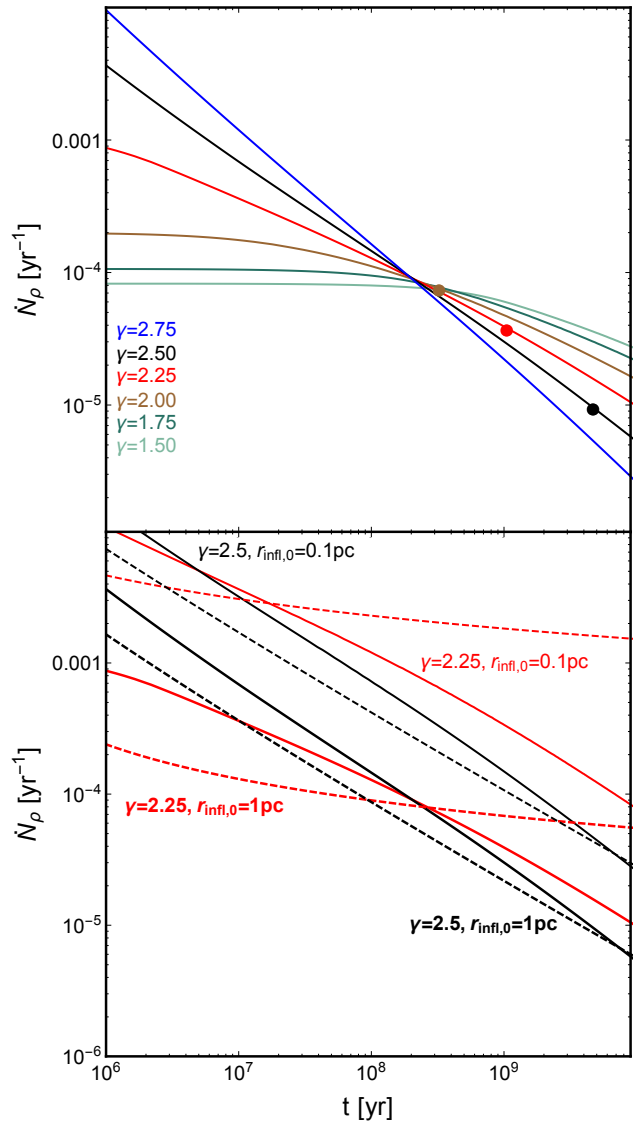


Figure 3. TDE rates as functions of time, for different initially overdense stellar density profiles, as calculated numerically by PHASEFLOW around a $M_\bullet = 10^6 M_\odot$ SMBH. *Top panel:* the power law slope of the density profile is varied, while the initial influence radius is fixed at 1 pc. Circles indicate the time when the initial influence radius $r_{\text{infl},0}$ is overtaken by the expanding r_{BW} , for initial $\gamma > 7/4$. *Bottom panel:* the effect of decreasing the influence radius to 0.1 pc is shown for ultrasteep profiles. Black curves are ultrasteep $\gamma = 2.5$ profiles, while red curves are more marginal $\gamma = 2.25$ profiles. Thick (thin) lines show $r_{\text{infl},0} = 1 \text{ pc}$ ($r_{\text{infl},0} = 0.1 \text{ pc}$). Numerical solutions are solid lines, while the analytic rates from Eq. 4 are plotted as dashed lines. As in Fig. 2, a good fit in time evolution is seen for ultrasteep profiles, but this breaks down for marginally ultrasteep $\gamma = 2.25$ cusps. The analytic normalization is off by a factor of a few from numerical results.

delay time distribution $\dot{N}_\rho(t)$ is controlled by the initial power law slope γ . When γ is in the ultrasteep regime, our analytic formula for the DTD (Eq. 5) describes its time evolution well. We defer a more detailed discussion of these considerations for §5.

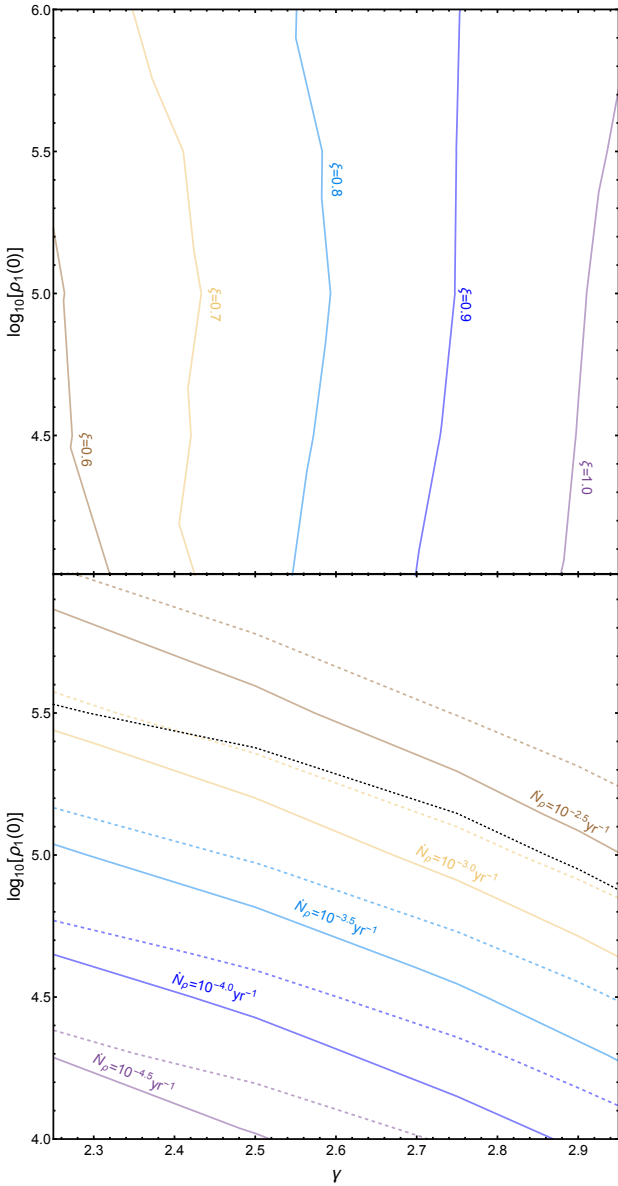


Figure 4. *Top panel:* The time evolution of the TDE rate is well approximated by a power-law $\dot{N}_p \propto t^{-\xi}$, for initial stellar density profiles $\rho \propto r^{-\gamma}$ in the ultra-steep regime $\gamma \geq 9/4$ (eq. 5). Here we show contours of ξ as a function of γ , measured by averaging our numerical results over the time interval $10^8 \text{ yr} < t < 10^{10} \text{ yr}$. *Bottom panel:* Contours of the TDE rate at $t = 100$ Myr (solid lines) and 200 Myr (dashed lines) as a function of the initial stellar density profile γ and the normalization of the initial stellar density profile, $\rho_1(0) \equiv \rho(t=0, r=1 \text{ pc})$. Above the black dotted line, the central SMBH mass would double over 10 Gyr if it accreted half of each disrupted star (the effects of which are not included in our calculations).

3 RADIAL VELOCITY ANISOTROPIES

An alternative dynamical explanation for the PSP is a radial orbit bias among the stars formed in the center of a galaxy during a starburst⁶. Because stars on nearly radial orbits require far less time to diffuse through angular momentum space into the SMBH loss

⁶ The effect of radial anisotropies on TDE rates was first commented on in Magorrian & Tremaine (1999).

cone, a stellar cluster born with a radial velocity anisotropy will see an initially elevated TDE rate (relative to an otherwise equivalent cluster with an isotropic velocity field). However, the same two-body relaxation process that feeds stars to the SMBH also acts to isotropize the velocity distribution. Tangential velocity anisotropies have been explored previously as a mechanism to suppress TDE rates (Lezhnin & Vasiliev 2015, 2016); these investigations generally find that their anisotropies wash out in a fraction of an energy relaxation time. We expect that an initially radial velocity-space bias will also isotropize in a fraction of a relaxation time.

It is not obvious why a starburst would bias nuclear orbits in a radial sense (indeed, the disks of young stars seen in the Galactic Center have a pronounced tangential anisotropy, e.g. Bartko et al. 2009). We speculate that the infall and tidal disruption of young massive clusters could inject a fresh population of stars onto radial orbits in a post-starburst galactic nucleus, but modeling the full history of nuclear starbursts is beyond the scope of this paper. In this section, we simply investigate the self-consistent evolution of DFs with an initial radial bias, calculating the magnitude and duration of any enhancement to TDE rates therein.

We model the time evolution of the TDE rate in a galaxy with anisotropic stellar velocities by solving the time-dependent, one-dimensional Fokker-Planck equation in angular momentum space. By assumption, stars are fixed in bins of orbital energy, but allowed to diffuse through angular momentum space in a random walk. This process is captured by the orbit-averaged Fokker-Planck equation (Merritt & Wang 2005),

$$\frac{\partial f}{\partial \tau} = \frac{1}{4j} \frac{\partial}{\partial j} \left(j \frac{\partial f}{\partial j} \right), \quad (11)$$

where $j \equiv J/J_c(\epsilon)$ is the dimensionless angular momentum (here $J_c(\epsilon)$ is the specific angular momentum of a circular orbit), $\tau \equiv \bar{\mu}(\epsilon)t \sim t/t_r$ is a dimensionless time, and $\bar{\mu}(\epsilon)$ is the orbit-averaged angular momentum diffusion coefficient (see §2). We again assume a spherical geometry for the star cluster, and a separable distribution function $f(\epsilon, j) = f_\epsilon(\epsilon)f_j(j)$. The latter assumption - evolving j at fixed ϵ - is valid on timescales short compared to the energy relaxation time because angular momentum relaxation is much faster than energy relaxation for the radial orbits that concern us. However, Eq. 11 will break down at late times, once either

- (i) An energy relaxation time has passed, and $f_\epsilon(\epsilon)$ can no longer be treated as static, or
- (ii) An order unity fraction of stars with specific energy ϵ have drained into the SMBH loss cone.

The outer boundary condition for Eq. 11 is of the Neumann type to prohibit flux of stars through $j = 1$:

$$\left. \frac{\partial f_j}{\partial j} \right|_{j=1} = 0. \quad (12)$$

The inner boundary condition depends greatly on the dimensionless diffusivity parameter $q(\epsilon) = P(\epsilon)\bar{\mu}(\epsilon)/j_{LC}^2(\epsilon) \approx \Delta J^2/J_{LC}^2$, where $j_{LC} \equiv \sqrt{2GM_\bullet R_t}/J_c(\epsilon)$ and $P(\epsilon)$ is the orbital period. In the strongly diffusive regime ($q \ll 1$, also known as the “empty loss cone” regime), stars are immediately destroyed once reaching $j = j_{LC}$ and the inner boundary condition is of the Dirichlet type: $f(j_{LC}, t) = 0$. However, in the pinhole regime ($q \gg 1$, also known as the “full loss cone” regime), relaxation can cause stars to wander to values of $j < j_{LC}$ many times per orbit and the loss cone is not empty. In this case the inner boundary condition is of the Robin

type (Vasiliev & Merritt 2013; Lezhnin & Vasiliev 2015),

$$f_j(j_{LC}) = \frac{\alpha(q)j_{LC}}{2} \left. \frac{\partial f_j}{\partial j} \right|_{j=j_{LC}}, \quad (13)$$

where $\alpha(q) \equiv (q^2 + q^4)^{1/4}$.

Following standard conventions, we parametrize the velocity anisotropy as

$$\beta \equiv 1 - \frac{T_{\perp}}{2T_{\parallel}}, \quad (14)$$

where T_{\perp} and T_{\parallel} are the kinetic energies of tangential and radial motion, respectively, integrated across the stellar distribution function. If all orbits are purely radial, then $\beta = 1$; if all orbits are purely tangential, then $\beta = -\infty$. An isotropic distribution corresponds to $\beta = 0$, so for the remainder of this section we focus on scenarios where $\beta > 0$, corresponding to a radial velocity bias. This parametrization of anisotropy maps onto the distribution function simply, with $f_j(j) \propto j^{-2\beta}$. As initial conditions, we therefore take⁷

$$f_j(j, t = 0) = \frac{1 - \beta_0}{1 - j_{LC}^{2-2\beta_0}} j^{-2\beta_0}, \quad j_{LC} < j \leq 1. \quad (15)$$

For convenience we have normalized the distribution function to unity, though this choice is inessential, as our interest is in studying the *relative* enhancement of the TDE rate (and its time evolution) due to a radial velocity bias in comparison to an isotropic velocity distribution.

For simplicity, we also assume in this section that the initial anisotropy β_0 is constant across all orbital energies ϵ . An upper limit on the allowed range of β_0 is set by the radial orbit instability (ROI). If the radial anisotropy exceeds some critical value β_{ROI} , the stellar system will become unstable to nonspherical perturbations, and the geometry of the star cluster will evolve into a nonspherical configuration (Antonov 1973; Henon 1973). Such a configuration will enhance TDE rates further (at least temporarily) through collisionless effects (Merritt & Poon 2004), but because the orbital dynamics and evolution of the distribution will become considerably more complicated, we defer an investigation of this scenario to future work. Although analytic criteria have suggested that $\beta_{ROI} \approx 0.43$ (Polyachenko & Shukhman 1981), numerical orbit integrations find stability up to larger anisotropies, with $\beta_{ROI} \approx 0.6$ (Merritt & Aguilar 1985). While the precise ROI threshold depends somewhat on the shape of the potential (and the distribution of anisotropies, which can of course differ from the power law ansatz in Eq. 14), we explore a large range of β_0 , with the caution that the most anisotropic models may not be self-consistent. Other dynamical instabilities may arise for non-monotonic $f_j(j)$ (Polyachenko et al. 2008), but we defer a discussion of this constraint for future work.

Since the approximate timescale for angular momentum relaxation to occur is $t_l(j) \approx j^2 t_r$, we expect radially biased initial conditions to relax from the inside out in angular momentum space, analogous to energy space relaxation in ultrastep cusps. We can likewise compute the range of angular momenta that have collisionally relaxed at some time t after the initialization of radially anisotropic initial conditions. In analogy to the ‘‘Bahcall-Wolf energy’’ ϵ_{BW} of §2, we find a ‘‘Cohn-Kulsrud angular momentum’’

$$j_{CK} \approx \sqrt{t}, \quad (16)$$

⁷ In order for our initial conditions to match the outer boundary condition, we select initial conditions that deviate very slightly from Eq. 15. Specifically, for $j > 0.999$, we set the initial DF to a constant value equal to $f(0.999, t = 0; \epsilon)$.

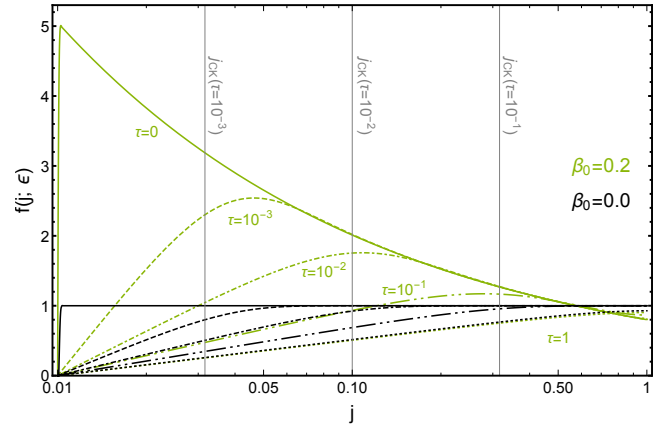


Figure 5. Evolution of the distribution function $f(j; \epsilon)$ as a function of the dimensionless angular momentum j at fixed energy ϵ , shown for different snapshots in dimensionless time $\tau = 0$ (solid), $\tau = 10^{-3}$ (dashed), $\tau = 10^{-2}$ (dot-dashed), $\tau = 10^{-1}$ (dot-dot-dashed) and $\tau = 1$ (dotted). Black lines correspond to an isotropic stellar cluster ($\beta_0 = 0$), while light lines show a case with moderate initial radial anisotropy ($\beta_0 = 0.2$). All cases assume a loss cone boundary condition $j_{LC} = 10^{-2}$ and a diffusive regime of LC repopulation ($q = 0.01$). The last snapshot, though technically beyond the domain of validity of our one-dimensional Fokker-Planck calculation, is shown for completeness.

interior to which the angular momentum DF should reach a steady state solution similar to Cohn & Kulsrud 1978 (here τ is the dimensionless time introduced after Eq. 11).

Fig. 5 shows the time evolution of the distribution function for an initially radially-biased profile with $\beta_0 = 0.2$, as compared to the standard isotropic case $\beta_0 = 0$, for $j_{LC} = 10^{-2}$ (an unusually large value chosen only for convenience of plotting). We find that the radially biased-initial conditions result in more stars being retained on low angular momentum orbits until roughly a relaxation time has passed (after which point the one-dimensional Fokker-Planck approach used is no longer valid). The time evolution of $f(j, t; \epsilon)$ is to zeroth order captured by Eq. 16; radially anisotropic initial conditions approach their logarithmic, steady state solution (Cohn & Kulsrud 1978) interior to a value of j that is within a factor of two of j_{CK} . For $j \geq j_{CK}$, the DF has not greatly evolved from its initial conditions. We therefore expect an enhanced flux of stars into the loss cones for all times $\tau < 1$ during which our calculation is valid.

The instantaneous loss cone flux is calculated as

$$\mathcal{F}(t; \epsilon) = 2\pi^2 \bar{\mu}(\epsilon) P(\epsilon) J_c^2(\epsilon) f_c(\epsilon) \left(j \frac{\partial f_j(j, t)}{\partial j} \right)_{j=j_{LC}}. \quad (17)$$

For our initial conditions, the TDE rate from a given energy bin, $\mathcal{F}(t; \epsilon)$, will be proportional to $f_j(j_{CK}, t)$ (as it is the Cohn-Kulsrud angular momentum which determines the slope of the DF into the loss cone), implying the surprisingly simple time evolution

$$\dot{N}_{\beta}(t) \propto t^{-\beta_0}. \quad (18)$$

Fig. 6 shows the time evolution of the diffusive loss cone flux enhancement $\mathcal{F}(t; \epsilon) / \mathcal{F}_{iso}(t; \epsilon)$ for different degrees of anisotropy $\beta_0 = 0.1 - 0.6$ and two assumptions about the loss-cone angular momentum ($j_{LC} = 10^{-5}, 10^{-2}$), normalized to the otherwise equivalent flux for isotropic ($\beta_0 = 0$) initial conditions, $\mathcal{F}_{iso}(t; \epsilon)$. Larger values of j_{LC} correspond to stars tightly bound to the SMBH (high values of ϵ), while smaller values represent those near the radius of influence of a low-mass SMBH (lower values of ϵ). Results for the pinhole regime are very similar and are not shown. Note that all

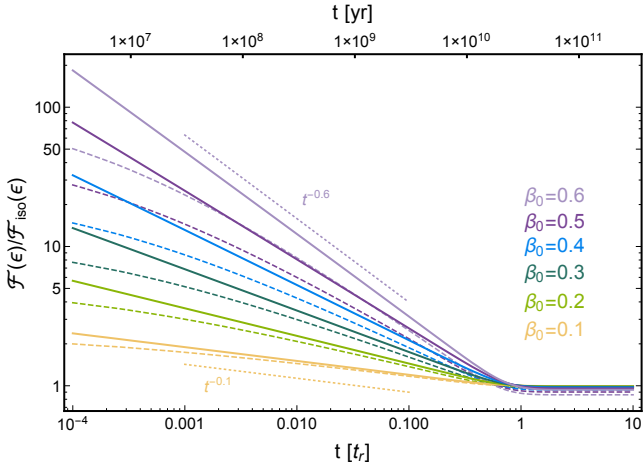


Figure 6. Time evolution of the flux of stars into the SMBH loss cone, \mathcal{F} , normalized to the equivalent stellar flux for isotropic initial conditions, \mathcal{F}_{iso} . Curves represent numerical solutions to Eq. 11. Time on the lower horizontal axis is normalized to the relaxation time t_r ; on the upper axis we show the physical passage of time for a low-mass cusp galaxy with $M_\bullet = 10^{6.5} M_\odot$ and $\gamma = 1.6$. We consider a range of different anisotropic initial conditions, with $\beta_0 = 0.1$ (yellow), 0.2 (light green), 0.3 (dark green), 0.4 (blue), and 0.5 (purple), and 0.6 (lavender). The largest β_0 values may trigger the onset of the radial orbit instability, limiting the validity of those calculations. Solid lines represent energy bins near the influence radius from where most TDEs are sourced ($j_{\text{LC}} = 10^{-5}$) while dashed lines represent much more tightly bound stellar orbits ($j_{\text{LC}} = 10^{-2}$); in both cases we consider strongly diffusive ($q = 0.01$) LC repopulation. Dotted lines show analytic power law estimates $\dot{N} \propto t^{-\beta_0}$ (Eq. 18), which are generally in excellent agreement with our numerical solutions.

energy dependent quantities in $\mathcal{F}(t; \epsilon)/\mathcal{F}_{\text{iso}}(t; \epsilon)$ cancel out (aside from the value of j_{LC} used to solve Eq. 11).

In Fig. 6, we see that an initial radial anisotropy enhances the TDE rate by a factor ≈ 2 –200 compared to the otherwise equivalent isotropic case. The rate declines as a power law in time that (for $j_{\text{LC}} \ll 1$) is well described by Eq. 18. The upper horizontal axis of Fig. 6 shows time in years for a $10^{6.5} M_\odot$ SMBH with “typical” values of $r_{\text{infl}} = 1.5$ pc and $\gamma = 0.61$ (these values are estimated by fitting power laws to the distributions of γ and r_{infl} estimated from the galaxy sample of Stone & Metzger 2016; see §5). For a very high initial anisotropy, $\beta_0 = 0.6$, we find that a system of age $t = 10^8$ yr will have a rate enhancement ≈ 50 . If the ROI limits β_0 to values ≤ 0.5 , the enhancement is reduced to ≤ 20 .

The TDE rate under radially-biased conditions eventually falls below the isotropic one as stars are depleted from the DF; this occurs after a time $\tau \sim 1$. However, this also marks the point after which the one-dimensional Fokker-Planck equation can no longer be trusted because energy space diffusion has become important. By this point, the distribution is largely isotropic and further evolution in the TDE rate occurs on the longer timescale for energy relaxation.

So far we have considered only the evolution of the angular momentum distribution $f_j(j)$ at fixed orbital energy ϵ . In typical, non-ultrasteep galaxies ($\gamma < 9/4$) with isotropic DFs, the integrated LC flux is sharply peaked at energies $\epsilon \approx \epsilon_{\text{crit}}$ (Wang & Merritt 2004); naively, this might imply that we could estimate the TDE rate in a radially anisotropic galaxy by considering the evolution of $f(j; \epsilon_{\text{crit}})$ alone. To test this hypothesis we integrate Eq. 11 numerically in many different bins of orbital energy across a distribu-

tion function $f(\epsilon)$. The total TDE rate $\dot{N}_\beta(t) = \int \mathcal{F}(t; \epsilon) d\epsilon$, where $\mathcal{F}(t; \epsilon)$ is given by Eq. 17.

We construct a grid of galaxy models varying M_\bullet between $10^5 M_\odot$ and $10^8 M_\odot$, and initial anisotropy parameter β_0 between 0.0 and 0.6. Each stellar system is idealized as a Dehnen model (Dehnen 1993; Tremaine et al. 1994): a spherical potential-density pair with a density profile $\rho(r)$ that is a smoothly broken power law. The inner region controls the TDE rate and has a power law density slope γ determined by least-squares fitting to the galaxy sample of Stone & Metzger (2016). The fit we find is $\gamma = 2.4997 - 0.1371 \log_{10}(M_\bullet/M_\odot)$; likewise, we set the break radius by assuming the galaxy’s total stellar mass $M_\bullet = 10^3 M_\bullet$, and that the influence radius follows the empirical scaling relation (Stone & Metzger 2016)

$$r_{\text{infl}} = 16 \text{ pc} \left(\frac{M_\bullet}{10^8 M_\odot} \right)^{0.69}. \quad (19)$$

The DF $f_\epsilon(\epsilon)$ is calculated numerically using Eddington’s integral (considering both the stellar and the SMBH potential). While Eddington’s integral is strictly valid only for isotropic stellar systems, and overestimates $f_\epsilon(\epsilon)$ for radially biased systems, we find that the net effect on the TDE rate is small. An example family of runs from this grid, with $\beta_0 = 0.5$, is shown in Fig. 7. We see that galaxy-integrated rate enhancements $\mathcal{R}_\beta(t) \equiv \dot{N}_\beta(t)/\dot{N}_{\text{iso}}(t)$ are the smallest, and wash out the fastest, for low mass galaxies. This is almost entirely understandable in terms of the longer relaxation times in high mass galaxies: for a fixed physical post-starburst age t , a $M_\bullet = 10^8 M_\odot$ galactic nucleus will have elapsed much less dimensionless time τ than a galactic nucleus with $M_\bullet = 10^6 M_\odot$. Of course, a countervailing effect is that the high mass SMBHs with the largest anisotropic rate enhancements are less common than their low mass counterparts; we return to this competition in §5.

Interestingly, our hypothesis that most flux into the LC originates from orbital energies $\epsilon \approx \epsilon_{\text{crit}}$ is incorrect. LC flux is much less steeply peaked for highly anisotropic systems ($\beta > 0$) than it is for isotropic ones, and a large portion of TDEs in radially biased galactic nuclei originate from physical scales $r \gg r_{\text{infl}}$. The reason for this is that the “full loss cone flux” which sets an upper limit on TDE rates in isotropic galactic nuclei,

$$\mathcal{F}_{\text{full}}^{\text{iso}}(\epsilon) d\epsilon = 4\pi^2 f(\epsilon) J_{\text{LC}}^2(\epsilon) d\epsilon, \quad (20)$$

drops off steeply as one moves to energies $\epsilon < \epsilon_{\text{crit}}$. While an isotropic spherical system cannot produce LC fluxes greater than $\mathcal{F}_{\text{full}}^{\text{iso}}$, an anisotropic one can; its equivalent upper limit on LC flux is

$$\mathcal{F}_{\text{full}}(\epsilon) d\epsilon \approx 4\pi^2 f(\epsilon) J_{\text{LC}}^2(\epsilon) j_{\text{LC}}^{-2\beta}(\epsilon) d\epsilon \quad (21)$$

provided the $f_j(j)$ DF is described well by Eq. 15 down to values of j near j_{LC} . For $\beta > 0$, Eq. 21 declines less steeply for $\epsilon < \epsilon_{\text{crit}}$ than does Eq. 20, allowing stars from well beyond the critical radius to contribute significantly to the TDE rate. This raises the possibility that resolved spectroscopy and Schwarzschild modeling of nearby E+A galaxies could directly test the premise of this solution to the PSP, but we defer a detailed investigation of this prospect for future work.

In summary, radial orbital biases among the stars deposited in galactic nuclei following a starburst can provide large enhancements to TDE rates (up to ~ 100), which wash out over an energy relaxation time. Larger galaxies are more promising hosts for these rate enhancements because of their longer relaxation times. For a stellar density profile $\rho(r) \propto r^{-\gamma}$, the radial anisotropy erodes from the inside out if $\gamma > 3/2$, and from the outside in if $\gamma < 3/2$.

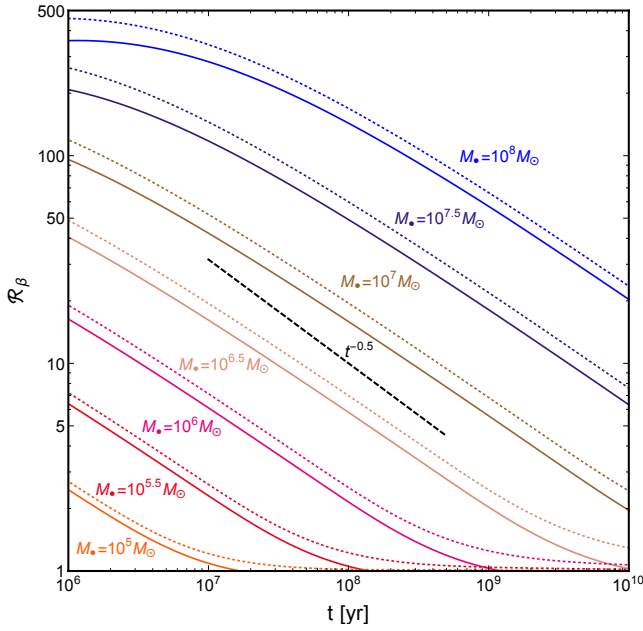


Figure 7. TDE rate enhancements $\mathcal{R}_\beta(t) \equiv \dot{N}_\beta(t)/\dot{N}_{\text{iso}}(t)$ in idealized galactic models with initial radial bias $\beta_0 = 0.5$, plotted against physical post-starburst age t . Solid lines compute TDE rates $\dot{N}_\beta(t)$ by integrating across a DF $f_e(\epsilon)$ computed from Eddington’s formula, while dotted lines use a DF $f_e(\epsilon)$ that is derived self-consistently. The difference is small, $\approx 20\%$. Different colors correspond to different SMBH and host galaxy masses; the SMBH masses M_\star are labeled in the figure. The dashed black line is a power law going as $t^{-0.5}$, as in Eq. 18. This analytic estimate for the anisotropic DTD is still a reasonable approximation, but it is less precise here than it was in Fig. 6, where only single bins of orbital energy ϵ were considered.

Regardless of the value of γ , the anisotropy among stars of *fixed energy* erodes from the inside out in j -space. In observed TDE galaxies, of age $t \gtrsim 10^8$ yr, rate enhancements can be large enough to explain observations if large initial values of β_0 do not trigger the radial orbit instability. We provide a more detailed comparison to observations in §5.

4 SMBH BINARIES

Several studies have demonstrated that the dynamical presence of a SMBH binary in a galactic nucleus can enhance rates of tidal disruption by several orders of magnitude, relative to an otherwise similar nucleus with a single, stationary SMBH. TDE rates are enhanced by the Kozai-Lidov mechanism (Ivanov et al. 2005) and by chaotic three-body scatterings (Chen et al. 2009), though the latter effect appears to dominate (Chen et al. 2011). Because E+A and post-starburst galaxies are often the result of galaxy mergers, a TDE rate enhancement driven by SMBH binarity offers a tempting explanation for the observed PSP (Arcavi et al. 2014).

One potential issue with this explanation is that the duration of TDE enhancement by the SMBHB is very short, $\sim 10^{5-6}$ yr. Although the TDE rate temporarily increases once a SMBH binary forms, as the SMBH binary ejects or tidally disrupts most of the stars within the influence radius of the primary SMBH, binary hardening stalls and the TDE rate plummets to levels far below that of a standard galactic nucleus (Chen et al. 2008). By combining dynamical estimates of the number of TDEs per SMBHB merger with approximate galaxy merger rates, Wegg & Bode (2011) estimate

that SMBHBs contribute only $\sim 2\%$ of the total number TDEs over cosmic times, insufficient to explain the observed PSP. However, given the many uncertainties in the calculation of Wegg & Bode (2011), this channel deserves further exploration.

In this section, we calculate the total TDE rate due to SMBHBs, in order to assess this scenario’s overall viability as an explanation for the PSP. Although the DTD itself is harder to quantify in this case than in the others we have considered thus far (§2, §3), we nevertheless estimate it in a limiting case.

4.1 TDE Rate from SMBHBs

Estimating the SMBH contribution to the TDE rate requires several pieces of information from astrophysical modeling and observations, which we first review before describing the calculation itself:

(i) The rate of galaxy mergers at redshift z is estimated using the following fitting formula taken from the cosmological Illustris Simulation (Rodríguez-Gomez et al. 2015):

$$\frac{dN}{dQ_\star dt} = A(z) \left(\frac{M_\star}{10^{10} M_\odot} \right)^{\alpha(z)} \left[1 + \left(\frac{M_\star}{2 \times 10^{11} M_\odot} \right)^{\delta(z)} \right] \times Q_\star^{\beta(z) + \gamma \log_{10}(M_\star / (10^{10} M_\odot))}, \quad (22)$$

where M_\star is the stellar mass of the larger galaxy and $Q_\star < 1$ is the (stellar) mass ratio of the merger. The fitted constants and functions in this equation are compiled in Appendix B.

(ii) The SMBH mass M_\bullet in each galaxy is calculated from the galactic bulge mass M_{bulge} using the Kormendy & Ho (2013) calibration of the $M_\bullet - M_{\text{bulge}}$ relationship, as

$$M_\bullet = 0.49_{-0.05}^{+0.06} \times 10^9 M_\odot \left(\frac{M_{\text{bulge}}}{10^{11} M_\odot} \right)^{1.16 \pm 0.08}. \quad (23)$$

We estimate M_{bulge} from the galaxy stellar mass M_\star using a bulge to total (B/T) relation from the mock galaxy catalog of van Velzen (2017), as provided in tabular form in Appendix B. The latter agrees qualitatively with similar work from the SDSS sample of Kim et al. (2016).

(iii) If the smaller merger partner also contains a SMBH (with a mass also given by the $M_\bullet - M_{\text{bulge}}$ relation and the above B/T prescription), then it will inspiral through dynamical friction to the center of the merger product, ultimately forming a SMBHB. This inspiral occurs on the dynamical friction timescale, which we estimate as (Taffoni et al. 2003)

$$T_{\text{DF}} = A \frac{x_0^2 R_h^2 V_h}{GM_s}, \quad (24)$$

where R_h is the virial radius of the primary galaxy’s halo, $V_h \equiv (GM_h/R_h)^{1/2}$ is the circular orbital speed at that location, $x_0 \equiv R_0/R_h$ (where R_0 is the initial orbital separation), and M_h (M_s) is the total halo mass of the primary (secondary) galaxy. A is a dimensionless constant defined in Appendix B, which depends on the properties of the merging galaxies (e.g. central density profile, concentration parameter of the halo), and, more uncertainly, on the properties of the merger: both orbital circularity $\varepsilon \leq 1$ and initial separation R_0 . Because $R_h \propto M_h^{1/3}$, $T_{\text{DF}} \propto Ax_0^2/Q_h$, where $Q_h \equiv M_s/M_h$. The extremely weak dependence of A on M_h (see Appendix B) renders T_{DF} almost completely independent of M_h when all other merger properties (e.g. Q_h , ε , x_0) are held fixed.

Because the TDE rate is enhanced only near the end of the dynamical friction inspiral, T_{DF} provides an estimate of the delay time between the merger and the epoch of TDE rate enhancement.

(iv) Finally, the total number of TDEs when forming a bound SMBHB is estimated as (Liu & Chen 2013)

$$N_{\text{TDE}} \approx \frac{7 \times 10^4}{(3 - \gamma)^{1/2}} Q^{(2-\gamma)/(6-2\gamma)} \left(\frac{M_\bullet}{10^7 M_\odot} \right)^{11/12}, \quad (25)$$

where $Q < 1$ is the SMBHB mass ratio computed from the galaxy mass ratio Q_\star using Eq. 23. This analytic result is empirically calibrated from the three-body scattering simulations of Chen et al. (2011), who computed TDE rates due to the perturbation of stellar orbits by the potential of a secondary SMBH in a galactic nucleus. The scalings entering this expression roughly agree with the independent work of Wegg (2013), although the latter simulations find a prefactor which is ≈ 5 times smaller. Our use of Eq. 25 therefore places an upper limit on the number of SMBHB-catalyzed TDEs, as the true number could be smaller by a factor of a few (though we note that both Chen et al. 2011 and Wegg 2013 consider SMBHBs in spherical star clusters; it is not yet known whether nonspherical geometries can enhance the total number of SMBHB-induced disruptions).

From the above information, we estimate the per-galaxy TDE rate at redshift z as the integral of the galaxy merger rate (Eq. 22) multiplied by the number of TDEs per merger (Eq. 25),

$$\dot{N}_{\text{SMBHB}}(M_\star, z) = \int_{Q_{\min}(z)}^1 \frac{dN}{dQ_\star dt} \Big|_{z_{\text{DF}}} N_{\text{TDE}}(M_\star, Q_\star) dQ_\star. \quad (26)$$

The lower limit of integration $0.01 \lesssim Q_{\min}(z) \lesssim 0.1$ is set by the lowest merger mass ratio capable of producing a SMBHB within the lookback time to when the merger took place. This is determined by equating the dynamical friction timescale (Eq. 24) to the lookback time between the observing redshift z and the redshift of the merger z_{DF} , considering only mergers that took place at $z_{\text{DF}} < 3$. The galaxy merger rate $dN/dQ_\star dt$ in Eq. (26) is evaluated at the unique merger redshift $z_{\text{DF}}(M_\star, Q_\star, z)$ which yields a SMBHB by the event redshift z (we compute z_{DF} by numerically solving Eq. 24 for z).

Fig. 8 shows the per-galaxy TDE rate \dot{N}_{TDE} as a function of the descendent SMBH mass M_\bullet at two characteristic redshifts, $z = 0.1$ (orange lines) and $z = 1$ (blue lines). One uncertainty in our calculation arises because we must make assumptions about the circularity $\varepsilon \leq 1$ of the merger and the initial orbital radius R_0 of the satellite galaxy, which enter into the dynamical friction timescale. Another uncertain parameter is the power law density slope γ of the primary's nuclear star cluster. The shaded error region in each curve brackets these uncertainties between an optimistic ($\varepsilon = 0.5$, $R_0 = 0.4R_h$, $\gamma = 1.9$) and a pessimistic ($\varepsilon = 0.9$, $R_0 = 0.8R_h$, $\gamma = 1.2$) case. Shown for comparison is a power-law fit to the average TDE rate as a function of SMBH mass, calculated from two-body scattering based on measured stellar density profiles from a large population of nearby galaxies (Stone & Metzger 2016).

The rate of TDEs arising from SMBHBs increases with increasing (primary) SMBH mass M_\bullet , as massive galaxies experience a moderately greater number of mergers than smaller ones (Eq. 22) and produce far more SMBHB-induced disruptions in each (Eq. 25). The TDE rate rolls over above the Hills mass⁸ of $M_H^{2/3} = R_\star c^2 / (2GM_\star^{1/3})$, the maximum mass SMBH that can produce visible flares from tidal disruption (Hills 1975). Since the vast

⁸ We compute population-averaged Hills masses following the prescription of Stone & Metzger (2016), i.e. assuming a Kroupa present-day mass function truncated above $M_\star = 1M_\odot$.

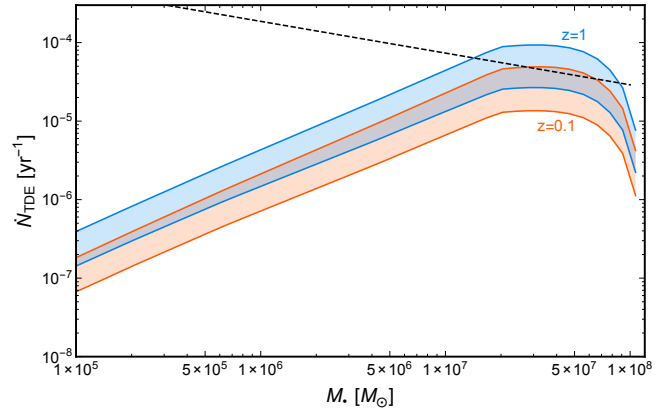


Figure 8. Cosmically-averaged per-galaxy TDE rate \dot{N}_{SMBHB} of the binary SMBH channel, as a function of the mass M_\bullet of the descendant SMBH. Orange and blue lines correspond to the rate at redshifts $z = 0.1$ and $z = 1$, respectively. Shaded regions denote the uncertainty range defined by adopting “optimistic” versus “pessimistic” values for uncertain parameters, such as the average circularity of the galaxy merger ($\varepsilon = 0.5$ or 0.9), initial merger radius ($R_0 = 0.4R_h$ or $0.8R_h$), and slope of the density profile of the nuclear star cluster ($\gamma = 1.9$ or 1.2). Averaged over the SMBH mass function, the local ($z = 0.1$) rates are far below those predicted in *typical* (non-SMBH binary hosting) galactic nuclei through two-body interactions, though they are competitive at the high mass end ($M_\bullet \gtrsim 10^7 M_\odot$). The best fit power law to the predicted two-body TDE rate of typical galaxies is shown as a black dashed line (Stone & Metzger 2016).

majority of binary-induced TDEs are caused by the primary SMBH (Wegg 2013), we only consider its Hills mass in our computations.

At $z = 0.1$ the per-galaxy rate of SMBHB-catalyzed TDEs is generally less than the $\dot{N} \sim 10^{-4} \text{ yr}^{-1}$ predicted by theory (Stone & Metzger 2016) and suggested by recent modeling of the observed TDE luminosity function (van Velzen 2017). However, the SMBHB-catalyzed TDE rate becomes competitive at the most massive end of TDE hosts ($M_\bullet \sim 10^{7.5} M_\odot$), and could under optimistic assumptions account for an order unity fraction of disruptions there. The SMBHB TDE rate in our model grows with redshift, increasing by a factor of a few from $z = 0.1$ to $z = 1$. However, because our model does not account for the uncertain redshift evolution of the $M_\bullet - M_{\text{bulge}}$ scaling relation, its predictions at high z should be taken with caution. That said, the redshift evolution of the SMBH mass function (cosmic downsizing) suggests that the TDE rate due to two-body relaxation could decline quickly with redshift, in which case the relative contribution of SMBHB TDEs may grow with z (Kochanek 2016).

By combining the per-galaxy TDE rate from SMBHBs with the local ($z \approx 0.1$) galaxy mass function of Stone & Metzger (2016), we estimate the volumetric TDE rate from the SMBHB channel to be $2.2 \times 10^{-7} \text{ Mpc}^{-3} \text{ yr}^{-1} < \dot{n} < 8.0 \times 10^{-7} \text{ Mpc}^{-3} \text{ yr}^{-1}$. While this range falls far below empirically-calibrated two-body TDE rate estimates of $\dot{n} \gtrsim 3.0 \times 10^{-6} \text{ Mpc}^{-3} \text{ yr}^{-1}$ (Stone & Metzger 2016), it is comparable to or larger than some observationally estimated rates (for example, van Velzen & Farrar (2014) estimate a volumetric rate of $\dot{n} = 4 - 8 \times 10^{-8 \pm 0.4} \text{ Mpc}^{-3} \text{ yr}^{-1}$). However, a recent analysis by van Velzen (2017) finds a higher TDE rate of $\dot{n} \approx 7.4 \times 10^{-7} \text{ Mpc}^{-3} \text{ yr}^{-1}$, which increases to $\dot{n} \approx 2.7 \times 10^{-6} \text{ Mpc}^{-3} \text{ yr}^{-1}$ if the actual TDE luminosity function extends just a factor of a few lower, to a value of $\approx 10^{42} \text{ erg s}^{-1}$, comparable to the dimmest observed flares.

If the broader TDE rate discrepancy indeed arises due to some combination of observational selection effects (e.g. dust extinction,

spectroscopic followup choices in optical surveys, a wide TDE luminosity function), such that theoretical rate estimates are roughly correct, then we conclude that SMBHBs are relegated to a sub-dominant channel for TDE production. They would in this case contribute at most 7.5 – 26% of the “normal rate” arising from two-body relaxation⁹, and are unlikely to explain the PSP. Alternatively, if something is wrong with standard two-body relaxation calculations (Wang & Merritt 2004; Stone & Metzger 2016), and lower observationally inferred rates are correct (Donley et al. 2002; van Velzen & Farrar 2014, but see also Esquej et al. 2008; Holoien et al. 2016), then TDEs sourced by SMBHBs may constitute an order unity fraction of the TDE sample, and thus may serve as viable explanations of the PSP. Regardless, we have found a somewhat higher fractional rate of SMBHB-induced TDEs than the $\approx 3\%$ estimated by Wegg & Bode (2011), though at least part of this difference stems from the different three-body scattering results found by Wegg & Bode (2011) versus those from Chen et al. (2011) used here.

Independent of these uncertainties on the total rate, one additional comparison to observations can be gleaned from Fig. 8 that appears to disfavor SMBHBs as a dominant TDE production channel. As noted earlier, most TDEs sourced from SMBHBs arise from primary SMBHs of mass $10^7 M_\odot \lesssim M_\bullet \lesssim 10^8 M_\odot$, a result which is robust to the observing redshift and choice of free parameters in our dynamical friction model. However, this result is in strong tension with the bottom-heavy SMBH mass distribution of TDE hosts found by (Wevers et al. 2017), based on a sample of twelve optically-selected TDEs. It is in less, but still noticeable, tension with the luminosity-weighted TDE host mass function constructed from this sample (van Velzen 2017).

4.2 The SMBHB DTD

The DTD for the SMBHB channel represents a convolution of two different delay times - the dynamical friction time T_{DF} (which determines the delay between the galaxy merger and the enhancement of the TDE rate due to SMBHB formation) and the delay between the galaxy merger and the starburst, ΔT_{burst} . While the former can be estimated (albeit with some uncertainties) from Eq. 24, the time delay between merger and starburst is much more uncertain, and ultimately must be determined from cosmological simulations.

Nevertheless, using the tools assembled here, we can still estimate the DTD in a highly idealized version of this scenario, in which the merger-starburst delay is much smaller than the delay between merger and SMBHB formation. In this limit, the fraction of SMBHB-triggered TDEs that occur before a post-starburst age t is given by

$$C(t; M_\star, z) = \frac{\int_{Q_{\min}(t,z)}^1 \frac{dN}{dQ_\star dt} \Big|_{z_{\text{DF}}} N_{\text{TDE}}(M_\star, Q_\star) dQ_\star}{\dot{N}_{\text{SMBHB}}(M_\star, z)}. \quad (27)$$

Here we have defined a more general $Q_{\min}(t, z)$ as the minimum galaxy mass ratio that will produce a SMBHB within a time $t < t_{\text{H}}$ of the merger itself.

Our results for this cumulative distribution, which represents the *time integral* of the DTD, is shown in Fig. 9, shown separately

⁹ The fraction of SMBHB-induced TDEs would be even lower if the occupation fraction of massive black holes with $M_\bullet \lesssim 10^6 M_\odot$ is high; this comparison assumes the conservative theoretical 2-body rate of $\dot{n} = 3.0 \times 10^{-6} \text{ Mpc}^{-3} \text{ yr}^{-1}$

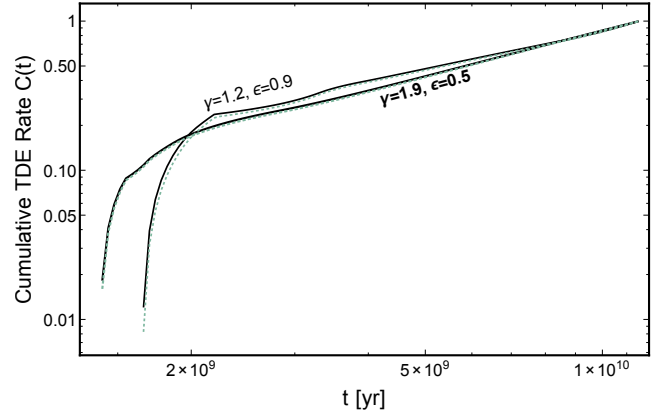


Figure 9. Cumulative distribution $C(t)$ of the local ($z = 0.1$) TDE rate induced by SMBHBs as a function of the post-merger age t . Thick/thin lines correspond, respectively, to optimistic/pessimistic choices of free parameters entering the SMBH rate calculation (see §4.1). Green dashed and black solid lines show results for primaries masses of $10^6 M_\odot$ and $10^7 M_\odot$, respectively. The strong similarities between these curves reflects how the primary mass scales out of Eq. 24, as explained in §4.1. The dearth of SMBHB-induced TDEs for post-merger ages $t < 10^9$ yr disfavors the SMBHB explanation for the PSP, which requires a rate enhancement on timescales $t \lesssim 10^8$ yr.

for SMBHBs with primary masses of $M_\bullet = 10^6, 10^7 M_\odot$. We observe that essentially no SMBHB-triggered TDEs occur at early times $t < 10^9$ yr after the galaxy merger. Therefore, unless the average delay between a galaxy merger and its starburst is fine-tuned to occur in the narrow window $\Delta T_{\text{burst}} \approx (0.9 - 1)T_{\text{DF}}$, there is no reason to expect a large fraction of TDEs should originate in galaxies with post-starburst ages $t \sim 10^8$ yr. Since the merger-starburst delay time is set by completely different physical processes than those that set T_{DF} , this requisite fine-tuning provides an additional argument against the SMBHB explanation for the PSP.

5 COMPARISON TO OBSERVATIONS

The previous sections outlined three dynamical explanations for the PSP, for two of which (the overdensity and radial anisotropy hypotheses) we have estimated theoretical DTDs. The DTD in the SMBHB case is difficult to estimate outside the framework of cosmological simulations, but as this scenario is disfavored on multiple grounds (insufficient overall rate, a top-heavy SMBH mass distribution, and required fine-tuning of the time delay ΔT_{burst} between galaxy merger and starburst), we do not consider it further. We begin this section by addressing the interaction between the post-starburst preference and a broader TDE rate dilemma (§5.1). Then, we compare our theoretical DTDs to the observational data collected by French et al. 2017 (§5.2).

5.1 TDE Rates

Two-body relaxation estimates of TDE rates in nearby galaxies generally find that (i) the total TDE rate is dominated by those from the lowest mass SMBHs that exist with a high occupation fraction¹⁰; (ii) under the assumption of a broad SMBH mass function, the average per-galaxy TDE rate is $\dot{N} \gtrsim 10^{-4} \text{ gal}^{-1} \text{ yr}^{-1}$ (Wang

¹⁰ But see also Brockamp et al. (2011).

& Merritt 2004; Stone & Metzger 2016). While the distribution of SMBH masses in optically-selected TDE hosts appears consistent with the first prediction (Wevers et al. 2017), the second prediction may be in significant tension with observations. The observed rate as inferred from X-ray-selected flares ranges from $\dot{N} = 9 \times 10^{-6} \text{ gal}^{-1} \text{ yr}^{-1}$ (Donley et al. 2002) to $\dot{N} = 2 \times 10^{-4} \text{ gal}^{-1} \text{ yr}^{-1}$ (Esquej et al. 2008). Rates inferred from optically-selected flares are also quite uncertain; the ASAS-SN survey, for instance, estimates a TDE rate of $\dot{N} = 2 - 17 \times 10^{-5} \text{ gal}^{-1} \text{ yr}^{-1}$ (Holoien et al. 2016).

An accurate rate estimate is challenging to obtain, due to uncertain survey selection effects; for example, in many time domain surveys, it is hard to quantify what criteria leads certain transients to receive the spectroscopic follow-up necessary to result in a TDE classification. Dust extinction may lead to an underestimation of the true TDE rate; conversely, the present TDE sample may be contaminated at some level with TDE impostors, such as nuclear supernovae (Saxton et al. 2016), unusually variable AGN (Komossa et al. 2015), or exotic types of stellar collisions (Metzger & Stone 2017). Ideally, rates should be estimated using a complete, flux-limited sample, but such an approach is hindered by the complicated selection functions that enter into most time domain surveys. Only the small number of SDSS-selected TDEs ($N = 2$) represents a truly flux-complete (down to a limiting peak TDE luminosity) sample, from which one infers a low rate of $\dot{N} = 0.2 - 4.7 \times 10^{-5} \text{ gal}^{-1} \text{ yr}^{-1}$ (van Velzen & Farrar 2014). However, the true TDE rate is probably higher than this: recent modeling of the optical TDE luminosity function indicates that large, generally unseen populations of faint TDEs could be biasing observational inferences. When the low detection rate of these faint TDEs is accounted for, one finds that they dominate the volumetric rate, and this yields a flux-corrected per-galaxy TDE rate $\dot{N} \approx 1 \times 10^{-4} \text{ gal}^{-1} \text{ yr}^{-1}$ (van Velzen 2017), potentially eliminating the tension with theoretical two-body rates.

The overall magnitude of the TDE rate discrepancy in normal (non post-starburst) galaxies remains an open question, but one that is important for using DTDs to discriminate between different dynamical explanations of the PSP. Because the bottom end of the TDE luminosity function remains poorly constrained, observational estimates of the PSP are most accurately expressed as *relative* rate enhancements \mathcal{R} as a function of post-starburst age, rather than in terms of the *absolute* per-galaxy rate \dot{N} . By making the reasonable assumption that the TDE luminosity function is the same in normal and post-starburst galaxies, this enables us to translate theoretical predictions of absolute TDE rates (e.g. §2) into predictions about relative rates, which we compare to data in the next subsection. However, we caution that this assumption (and thus our conclusions derived from it) could be invalid if the PSP arises due to non-dynamical effects, such as preferential dust obscuration in normal galaxies.

5.2 The Delay Time Distribution

French et al. (2016) found that 6 of 8 TDEs in their optical/UV-selected sample occurred in galaxies with strong Balmer absorption features, consistent with a starburst occurring $t_\star \sim 100$ Myr to 3 Gyr ago. Three of these are classical E+A galaxies, consistent with a recent starburst ($t_\star \sim 100 - 200$ Myr), while another three show weaker Balmer absorption features, consistent with a slightly older starburst with $t_\star \sim 0.3 - 3$ Gyr (but see also French et al. 2017 for caveats on the latter set of post-starburst ages). Only two TDEs in the sample occur in galaxies with old stellar populations $t_\star \gtrsim 1$ Gyr, implying a much lower per-galaxy TDE rate in this

population. By comparing the number of TDEs in each bin of post-starburst age to the frequency of these galaxy ages in SDSS data, and under the assumption that the TDE luminosity function (after absorption/extinction) is constant across galaxy types, one finds that the TDE rate is enhanced in E+A and more weakly Balmer-strong galaxies by factors of $\mathcal{R} = 190_{-100}^{+115}$ and $\mathcal{R} = 33_{-11}^{+7}$, respectively.

More recent work, accounting for possible selection effects and employing larger TDE candidate samples, has found smaller but still significant overrepresentations of post-starburst galaxies among TDE hosts (Law-Smith et al. 2017; Graur et al. 2017). In particular, Graur et al. (2017) used the same galaxy selection criteria as French et al. (2016), and found TDE rate enhancements in E+A and more weakly Balmer-strong galaxies of $\mathcal{R} = 36_{-18}^{+22}$ and $\mathcal{R} = 18_{-6}^{+8}$, respectively. However, the careful stellar population modeling of French et al. (2017) has found the most accurate post-starburst age estimates so far for TDE host galaxies, so we rely on this work in estimating the observational DTD. We split their sample of eight TDE hosts into three categories. First, two TDE hosts are not in post-starburst galaxies. Second, five TDE hosts have a “post-starburst age” (the age since the *end* of the burst) of 100 – 600 Myr. Finally, one TDE host has a post-starburst age within 600–1100 Myr. Under the assumption that these two equally sized age bins are equally represented in the 2.3% of low- z galaxies with significant H δ absorption (French et al. 2016), we estimate that for our “young” and “old” bins of post-starburst age, the rate enhancement factors are $\mathcal{R} = 54_{-20}^{+17}$ and $\mathcal{R} = 11_{-9,0}^{+20}$, respectively. Here the upper and lower limits are one- σ binomial confidence levels (Gehrels 1986).

A tidal disruption flare candidate was recently discovered (Tadhunter et al. 2017; Dou et al. 2017) in a starbursting ultra-luminous infrared galaxy (ULIRG). Although further observations are needed to substantiate the TDE origin of this event, its confirmation would suggest that TDE rates are even higher in actively starbursting galaxies, $\gtrsim 10^{-2} \text{ yr}^{-1}$. If the TDE rate in normal galaxies is $\dot{N} \sim 10^{-4} \text{ gal}^{-1} \text{ yr}^{-1}$, this implies a rate enhancement of $\mathcal{R} \gtrsim 100$ in starburst galaxies ($t_\star \sim 10^7$ yr). Given the still uncertain nature of the ULIRG flare, we do not focus on explaining this intriguing data point, but still present it for comparison.

In order to compare the observed rate enhancement to our theoretical predictions of the overdensity (§2) and radial anisotropy (§3) hypotheses, we must define M_\bullet -averaged rate enhancement factors $\langle \mathcal{R}_\rho(t) \rangle$ and $\langle \mathcal{R}_\beta(t) \rangle$, respectively. We do not compute an averaged rate enhancement for the SMBHB hypothesis (§4) because, as already discussed, this scenario cannot explain the PSP absent fine-tuning. These mass-averaged relative DTDs are calculated by integrating our earlier, mass-dependent DTDs $\dot{N}_\rho(t, M_\bullet)$ and $\dot{N}_\beta(t, M_\bullet)$ over the SMBH mass function $\phi(M_\bullet)$ according to

$$\langle \mathcal{R}_\rho(t) \rangle = \dot{n}_{\text{SM16}}^{-1} \int_{M_{\min}}^{M_{\max}} \dot{N}_\rho(t, M_\bullet) \phi(M_\bullet) d \log_{10}(M_\bullet) \quad (28)$$

$$\langle \mathcal{R}_\beta(t) \rangle = \dot{n}_{\text{SM16}}^{-1} \int_{M_{\min}}^{M_{\max}} \dot{N}_\beta(t, M_\bullet) \phi(M_\bullet) d \log_{10}(M_\bullet) \quad (29)$$

$$\dot{n}_{\text{SM16}} = \int_{M_{\min}}^{M_{\max}} \dot{N}_{\text{SM16}}(M_\bullet) \phi(M_\bullet) d \log_{10}(M_\bullet), \quad (30)$$

where we take an empirical $\phi(M_\bullet)$ from Shankar et al. 2009 (units of $\text{Mpc}^{-3} \text{ dex}^{-1}$). Specifically, we use their tabulated low-redshift ($z = 0.02$) mass function; as a check of robustness, we have compared it to a different $\phi(M_\bullet)$ derived from galaxy scaling relations (Stone & Metzger 2016) and found only modest changes to $\langle \mathcal{R}_\rho(t) \rangle$ and $\langle \mathcal{R}_\beta(t) \rangle$. As the limits of integration, we adopt fiducial values

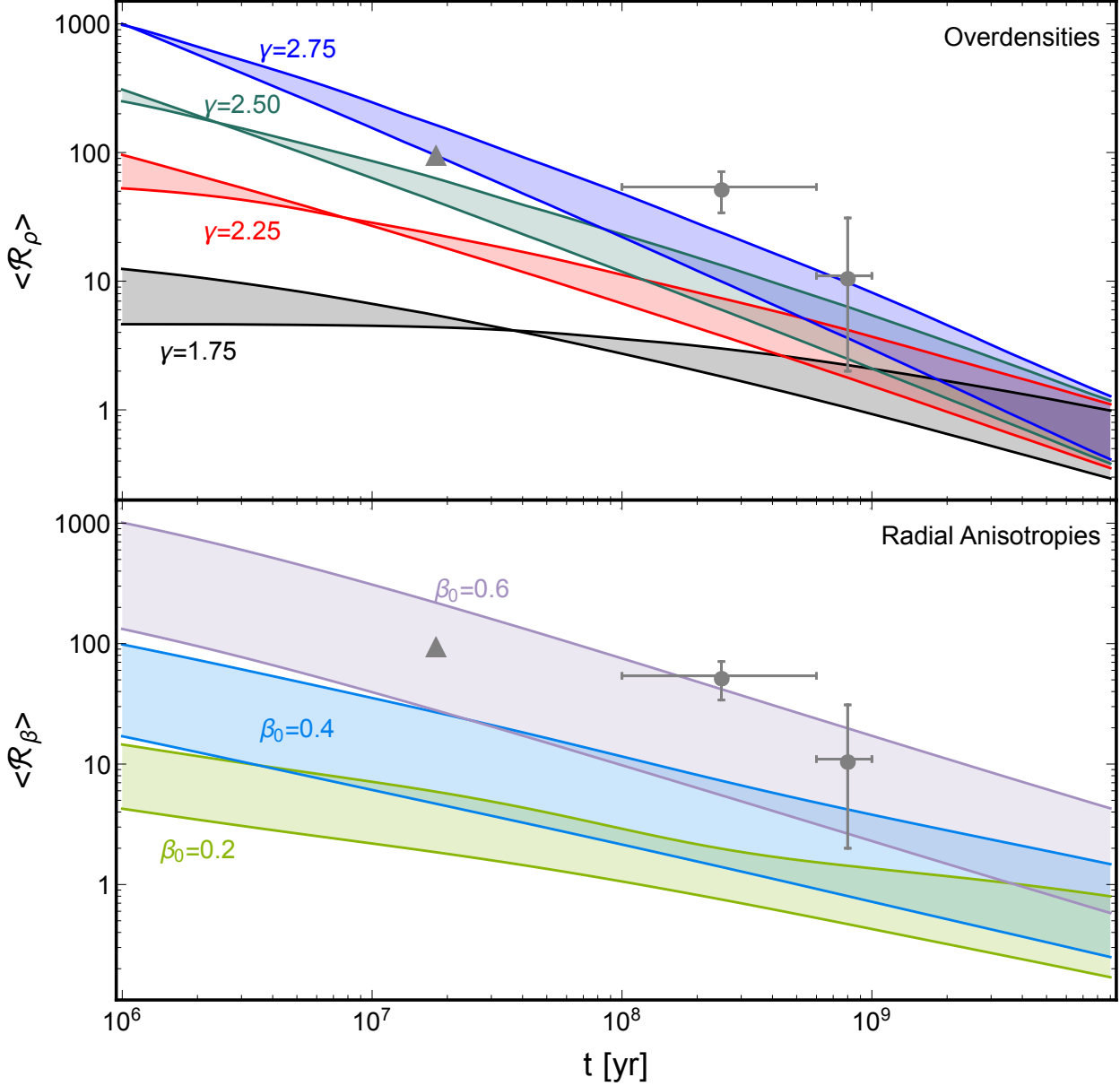


Figure 10. Theoretical delay time distributions showing TDE rate enhancements as a function of stellar age t of the nuclear star cluster. The rate enhancements in the overdensity and radial anisotropy explanations of the post-starburst TDE preference are compared to observational data from French et al. (2017), shown as gray circles. As DTDs must be integrated over the SMBH mass function, the shaded regions denote the uncertainties arising from whether we assume SMBH mass function to cut off below $M_{\bullet} = 10^5 M_{\odot}$ or $M_{\bullet} = 10^6 M_{\odot}$. A gray triangle shows the tentative TDE rate enhancement in starbursting galaxies, as inferred by the detection of a possible TDE in a ULIRG by Tadhunter et al. 2017 (though we caution that the TDE interpretation of this single event requires verification). *Top panel:* Rate enhancements $\langle \mathcal{R}_{\rho} \rangle$ for overdense post-starburst nuclei are shown. The black, red, green, and blue curves show the evolution of initial power law slopes $\gamma = 1.75$, $\gamma = 2.25$, $\gamma = 2.5$, and $\gamma = 2.75$, respectively. Each set of initial conditions has been given an initial normalization such that all Fokker-Planck simulations reproduce observed influence radii (Eq. 19) after 10^{10} yr of evolution. Observed post-starburst rate enhancements can be reproduced if $\gamma \geq 2.5$. *Bottom panel:* Rate enhancements $\langle \mathcal{R}_{\beta} \rangle$ for radially anisotropic post-starburst nuclei are shown. The lavender, cyan, and light green curves show time evolution of initial anisotropies $\beta_0 = 0.6$, $\beta_0 = 0.4$, and $\beta_0 = 0.2$, respectively. Observed post-starburst rate enhancements can be reproduced if $\beta_0 \geq 0.5$, which is close to the onset threshold of the radial orbit instability.

for the minimum and maximum SMBH mass of $M_{\min} = 10^6 M_{\odot}$ and $M_{\max} = 10^8 M_{\odot}$, respectively. Eqs. 28 and 29 are both normalized by a mass-integrated volumetric TDE rate \dot{n}_{SMB16} , which we calculate using the best-fit per-galaxy TDE rate of Stone & Metzger (2016),

$$\dot{N}_{\text{SMB16}}(M_{\bullet}) = 2.9 \times 10^{-5} \text{ gal}^{-1} \text{ yr}^{-1} \left(\frac{M_{\bullet}}{10^8 M_{\odot}} \right)^{-0.404}, \quad (31)$$

Fig. 10 compares the observed DTD to our mass-integrated theoretical predictions. The top panel shows the relative rate enhancement $\langle \mathcal{R}_{\rho}(t) \rangle$ in the overdensity hypothesis (§2) for different initial power law slopes γ and a range of minimum SMBH masses M_{\min} . The initial influence radii $r_{\text{infl},0}$ (or, equivalently, $\rho_1(0)$ values) are chosen so that the influence radius after 10^{10} yr of relaxation is equal to Eq. 19, yielding a standard galactic nucleus¹¹. This approach yields a realistic $\langle \mathcal{R}_{\rho}(10^{10} \text{ yr}) \rangle \approx 1$. Initial power law slopes $\gamma \gtrsim 2.5$ are capable of matching both post-starburst data points as well as the (very approximate) ULIRG data point.

Likewise, the bottom panel of Fig. 10 compares the observed DTD to the theoretical relative rate enhancement $\langle \mathcal{R}_{\beta}(t) \rangle$ in our anisotropic hypothesis (§3) for different initial anisotropies β_0 and a range of minimum SMBH masses M_{\min} . Lower values of M_{\min} always reduce $\langle \mathcal{R}_{\beta} \rangle$ at fixed post-starburst age t , because lower mass SMBHs have, on average, shorter relaxation times, in which case initial anisotropies wash out more quickly. As described earlier, larger values of β_0 lead to higher enhancements $\langle \mathcal{R}_{\beta} \rangle$. The anisotropic DTDs can match the observed rate enhancements for $\beta_0 \gtrsim 0.5$. Such large anisotropies lie close to the threshold for the radial orbit instability, and the viability of this hypothesis may depend on the nonlinear outcome of the ROI.

Most TDEs produced by overdense galactic nuclei come from low-mass SMBHs. The anisotropy hypothesis, on the other hand, is biased towards higher-mass SMBHs where relaxation times are long (see Fig. 7). Roughly half of the rate enhancement $\langle \mathcal{R}_{\beta}(t) \rangle$ in the bottom panel of Fig. 10 comes from SMBHs in the mass range $10^7 < M_{\bullet}/M_{\odot} < 10^8$. In this section we have cut off our integrals at a $M_{\max} = 1 \times 10^8 M_{\odot}$, in an approximation of the Hills mass. While the anisotropic explanation of the PSP does not favor as top-heavy a distribution of TDE hosts as the SMBHB scenario does (Fig. 8), more accurate modeling of the Hills mass, and perhaps SMBH spin distributions (Kesden 2012), may be necessary for future work to compare predicted SMBH mass distributions to observations (Wevers et al. 2017).

6 CONCLUSIONS

We have developed a new tool, the TDE *delay time distribution*, for studying the unusual host galaxy preferences of TDEs. This observable, already widely used in studies of other transients such

¹¹ In order to set realistic initial conditions, we ran an exploratory grid of PHASEFLOW models with a range of γ , $\rho_1(0)$ and M_{\bullet} values, and measured the final influence radii r_{infl} . These models were flattened to a $\rho \propto r^{-1/2}$ core inside a collision radius $\sim 10^{-2}$ pc set by Eq. 7, but our results are not sensitive to this flattening. We then interpolated across $\rho_1(0)$ (for fixed γ , M_{\bullet}) to estimate the $\rho_1(0)$ value that will yield Eq. 19, and used this value of $\rho_1(0)$ in a second grid of models across γ and M_{\bullet} . This second grid produced the DTDs used in Fig. 10. We find that an initial condition $\rho_1(0) = 0.617^{\gamma} \times 10^{6.32} M_{\odot} \text{ pc}^{-3} (M_{\bullet}/10^6 M_{\odot})^{-1.05+0.425\gamma}$ yields a final influence radius within a factor of two of Eq. 19.

as gamma ray bursts and Type Ia supernovae, may in the near future help discriminate between different explanations for the post-starburst preference of observed TDE flares. Most of these explanations are motivated by exotic stellar dynamical scenarios in the nuclei of post-starburst galaxies, and these scenarios generally have uncertain free parameters. DTDs are useful not only for discriminating between explanations of the PSP, but also for parameter extraction in the context of an individual dynamical hypothesis.

We have also investigated a new hypothesis for the PSP based on the assumption that starbursts in nuclear star clusters place stars onto preferentially radial orbits around the SMBH. Such radial orbits allow stars to diffuse rapidly into the loss cone, enhancing the TDE rate over that in an otherwise identical galactic nucleus with an isotropic stellar velocity field (to which the cluster relaxes at late times). By numerically solving the 1D (angular momentum) Fokker-Planck equation, we find that radial orbit anisotropies can enhance volumetric TDE rates by up to a factor of $\langle \mathcal{R}_{\beta} \rangle \approx 10 - 100$ (depending on the uncertain onset threshold of the radial orbit instability) on timescales of $\sim 10^8$ yr post-starburst. This enhancement, which declines approximately as a power law in time in each galaxy ($\dot{N} \propto t^{-\beta_0}$), provides a promising explanation for the PSP.

The overdensity hypothesis, proposed theoretically in Stone & Metzger (2016) and investigated empirically in Stone & van Velzen (2016), also appears capable of producing the large per-galaxy TDE rates observed in post-starburst galaxies. If the starburst produces an ultrasteep stellar cusp (initial power-law slope $\gamma \geq 9/4$) with a high density normalization, we find that large per-galaxy TDE rates of $\sim 10^{-3} \text{ yr}^{-1}$ are possible in nuclei with young stellar populations of age $\sim 10^8$ yr. The TDE rate declines steeply with time following the starburst, approximately as $\dot{N} \propto t^{-(4\gamma-9)/(2\gamma-3)} / \ln t$. When we choose initial density profile normalizations that, after 10^{10} yr of collisional evolution, reproduce observed nuclear properties (specifically, r_{infl}), we find that stellar profiles with initial power-law slopes $\gamma \gtrsim 2.5$ can reasonably reproduce the DTD implied by current data.

By contrast, the original hypothesis of Arcavi et al. (2014) - that the PSP may arise from a hidden population of SMBHBs - appears to contribute at most in a subdominant way to the observed rate enhancement. While a detailed delay time distribution for the SMBHB rate enhancement is beyond the scope of this paper, and likely can only be constructed from cosmological simulations, we have generated a simplified DTD for this scenario (Fig. 9). The SMBHB scenario is disfavored because dynamical friction sets a delay between galaxy merger and the formation of a hard SMBHB (i.e. the short-lived phase of TDE rate enhancement) that is typically $T_{\text{DF}} \gtrsim 1 \times 10^9$ yr. Unless the delay between galaxy merger and starburst, which is set by an entirely different set of hydrodynamical processes, is fine-tuned to be $\lesssim 10\%$ shorter than T_{DF} , then the SMBHB scenario cannot explain the PSP. Furthermore, by computing for the first time the distribution of primary SMBH masses in SMBHB-triggered TDEs, we have found a top-heavy distribution which is at odds with the bottom-heavy mass function of the observed TDE flare sample (Wevers et al. 2017).

While this paper provides a pioneering theoretical exploration of the TDE DTD, much additional work is needed to better characterize the time evolution of TDE rates. First, our investigations of the overdensity and radial anisotropy scenarios employed idealized 1D Fokker-Planck equations to study evolution in energy and angular momentum space, respectively. These calculations could be improved by solving the 2D Fokker-Planck equation, with the Monte Carlo method (e.g. Duncan & Shapiro 1983; Freitag & Benz 2002; Vasiliev 2015), or at much greater computational cost with

full N-body simulations (e.g. Brockamp et al. 2011; Wang et al. 2016). The latter two approaches could also help explore TDE rates in post-ROI systems born with high β_0 . Second, we have not attempted to compute the DTDs for more dynamically complex explanations of the PSP (e.g. a strongly triaxial geometry for post-starburst galactic nuclei, or secular dynamical processes in eccentric stellar disks). Third, we have largely ignored non-dynamical explanations of the PSP, such as preferentially low column depths in post-starburst galactic nuclei. If normal galaxies generally suffer from high levels of nuclear dust extinction (photoelectric absorption from neutral gas), the detectability of their optically (X-ray) bright TDEs will fall in contrast to less obscured galaxy subpopulations.

Finally, we note that the three different dynamical hypotheses in this paper - as well as other explanations of the PSP - may have another potential discriminant: the distribution of TDE impact parameters $\beta_{\text{TDE}} = R_i/R_p$. TDEs originating in SMBH binaries, or in triaxial stellar potentials, feed stars into the loss cone in the pinhole regime of disruption, in which a sample of TDEs will have an impact parameter distribution $N(\beta_{\text{TDE}}) \propto 1/\beta_{\text{TDE}}$. Conversely, the ultrasteep version of the overdensity hypothesis, which appears in some ways to be the most promising solution to the PSP, will be in the diffusive regime of disruption, in which most TDEs have $\beta_{\text{TDE}} \approx 1$ (though a minority of high β_{TDE} events will be supplied by strong scatterings - see Weissbein & Sari 2017). In the radial anisotropy scenario, the β_{TDE} distribution will depend on the details of the stellar density profile $\rho(r)$ and the initial anisotropy β_0 , but will generally favor the pinhole regime.

Our current knowledge of the PSP is limited by small number statistics: existing observations provide population ages for only a few dozen TDE host galaxies (French et al. 2016; Graur et al. 2017), and in many cases these ages are quite approximate (French et al. 2017). However, the sample of TDEs is expanding rapidly and will continue to do so as more time domain surveys, such as *ZTF* and the *LSST*, come online. As the stellar populations of more TDE hosts are characterized spectroscopically, it will become possible to construct empirical delay time distributions that distinguish increasingly subtle variations between the theoretical DTDs computed here. This will provide a straightforward test of different theoretical explanations for the peculiar host galaxy preference of TDEs, and other peculiar features of TDE demographics not yet identified.

ACKNOWLEDGMENTS

We gratefully acknowledge the assistance of Decker French in constructing the empirical DTD used in this paper, as well as fruitful discussions with Vicente Rodriguez-Gomez, Gregory Snyder, Paul Torrey, Sjoert van Velzen, and Ann Zabludoff. NCS received financial support from NASA through Einstein Postdoctoral Fellowship Award Number PF5-160145, and thanks the Aspen Center for Physics for its hospitality during the completion of this work. BDM and AG acknowledge support from NSF Astronomy and Astrophysics grants AST-1410950, AST-1615084; NASA Astrophysics Theory Program grants NNX16AB30G, NNX17AK43G; and Hubble Space Telescope Grant HST-GO-14785.004-A. EV acknowledges support from the European Research Council under the 7th Framework programme (Grant 321067).

REFERENCES

- Arcavi, I., Gal-Yam, A., Sullivan, M., et al. 2014, *ApJ*, 793, 38
 Antonov, V. A. 1973, *Dynamics of Galaxies and Star Clusters*, 139
 Auchettl, K., Guillochon, J., & Ramirez-Ruiz, E. 2017, *ApJ*, 838, 149
 Bahcall, J. N., & Wolf, R. A. 1976, *ApJ*, 209, 214
 Bahcall, J. N., & Wolf, R. A. 1977, *ApJ*, 216, 883
 Bartko, H., Martins, F., Fritz, T. K., et al. 2009, *ApJ*, 697, 1741
 Blagorodnova, N., Gezari, S., Hung, T., et al. 2017, arXiv:1703.00965
 Bloom, J. S., Giannios, D., Metzger, B. D., et al. 2011, *Science*, 333, 203
 Brockamp, M., Baumgardt, H., & Kroupa, P. 2011, *MNRAS*, 418, 1308
 Brown, G. C., Levan, A. J., Stanway, E. R., et al. 2015, *MNRAS*, 452, 4297
 Cenko, S. B., Krimm, H. A., Horesh, A., et al. 2012, *ApJ*, 753, 77
 Chen, X., Liu, F. K., & Magorrian, J. 2008, *ApJ*, 676, 54-69
 Chen, X., Madau, P., Sesana, A., & Liu, F. K. 2009, *ApJL*, 697, L149
 Chen, X., Sesana, A., Madau, P., & Liu, F. K. 2011, *ApJ*, 729, 13
 Chornock, R., Berger, E., Gezari, S., et al. 2014, *ApJ*, 780, 44
 Cohn, H., & Kulsrud, R. M. 1978, *ApJ*, 226, 1087
 Dehnen, W. 1993, *MNRAS*, 265, 250
 Donley, J. L., Brandt, W. N., Eracleous, M., & Boller, T. 2002, *AJ*, 124, 1308
 Dou, L., Wang, T., Yan, L., et al. 2017, *ApJL*, 841, L8
 Duncan, M. J., & Shapiro, S. L. 1983, *ApJ*, 268, 565
 Esquej, P., Saxton, R. D., Komossa, S., et al. 2008, *A&A*, 489, 543
 Franchini, A., Lodato, G., & Facchini, S. 2016, *MNRAS*, 455, 1946
 Freitag, M., & Benz, W. 2002, *A&A*, 394, 345
 French, K. D., Arcavi, I., & Zabludoff, A. 2016, *ApJL*, 818, L21
 French, K. D., Arcavi, I., & Zabludoff, A. 2017, *ApJ*, 835, 176
 Gehrels, N. 1986, *ApJ*, 303, 336
 Gezari, S., Martin, D. C., Milliard, B., et al. 2006, *ApJL*, 653, L25
 Gezari, S., Basa, S., Martin, D. C., et al. 2008, *ApJ*, 676, 944-969
 Gezari, S., Chornock, R., Rest, A., et al. 2012, *Nature*, 485, 217
 Graur, O., French, K. D., Zahid, H. J., et al. 2017, arXiv:1707.02986
 Guillochon, J., & Ramirez-Ruiz, E. 2013, *ApJ*, 767, 25
 Hayasaki, K., Stone, N., & Loeb, A. 2013, *MNRAS*, 434, 909
 Hayasaki, K., Stone, N., & Loeb, A. 2016, *MNRAS*, 461, 3760
 Henon, M. 1973, *A&A*, 24, 229
 Hills, J. G. 1975, *Nature*, 254, 295
 Holoien, T. W.-S., Prieto, J. L., Bersier, D., et al. 2014, *MNRAS*, 445, 3263
 Holoien, T. W.-S., Kochanek, C. S., Prieto, J. L., et al. 2016, *MNRAS*, 455, 2918
 Hung, T., Gezari, S., Blagorodnova, N., et al. 2017, arXiv:1703.01299
 Ivanov, P. B., Polnarev, A. G., & Saha, P. 2005, *MNRAS*, 358, 1361
 Kesden, M. 2012, *Phys. Rev. D*, 85, 024037
 Keshet, U., Hopman, C., & Alexander, T. 2009, *ApJL*, 698, L64
 Khabibullin, I., Sazonov, S., & Sunyaev, R. 2014, *MNRAS*, 437, 327
 Kim, K., Oh, S., Jeong, H., et al. 2016, *ApJ Supplements*, 225, 6
 Kochanek, C. S. 2016, *MNRAS*, 461, 371

Komossa, S. 2015, *Journal of High Energy Astrophysics*, 7, 148
 Komossa, S., Grupe, D., Saxton, R., & Gallo, L. 2015, arXiv:1502.06946
 Kormendy, J., & Ho, L. C. 2013, *ARA&A*, 51, 511
 Lauer, T. R., Faber, S. M., Gebhardt, K., et al. 2005, *AJ*, 129, 2138
 Law-Smith, J., Ramirez-Ruiz, E., Ellison, S. L., & Foley, R. J. 2017, arXiv:1707.01559
 Lezhnin, K., & Vasiliev, E. 2015, *ApJL*, 808, L5
 Lezhnin, K., & Vasiliev, E. 2016, *ApJ*, 831, 84
 Liu, F. K., & Chen, X. 2013, *ApJ*, 767, 18
 Lodato, G., King, A. R., & Pringle, J. E. 2009, *MNRAS*, 392, 332
 Loeb, A., & Ulmer, A. 1997, *ApJ*, 489, 573
 Madigan, A.-M., Halle, A., Moody, M., McCourt, M., & Nixon, C. 2017, arXiv:1705.03462
 Magorrian, J., & Tremaine, S. 1999, *MNRAS*, 309, 447
 Mandelbaum, R., Seljak, U., & Hirata, C. M. 2008, *JCAP*, 8, 006
 Merritt, D., & Aguilar, L. A. 1985, *MNRAS*, 217, 787
 Merritt, D., & Poon, M. Y. 2004, *ApJ*, 606, 788
 Merritt, D., & Wang, J. 2005, *ApJL*, 621, L101
 Merritt, D. 2013, *Dynamics and Evolution of Galactic Nuclei*, by David Merritt. ISBN: 9780691158600, Princeton: Princeton University Press, 2013
 Metzger, B. D., & Stone, N. C. 2016, *MNRAS*, 461, 948
 Metzger, B. D., & Stone, N. C. 2017, arXiv:1705.00643
 Moster, B. P., Naab, T., & White, S. D. M. 2013, *MNRAS*, 428, 3121
 Navarro, J. F., Frenk, C. S., & White, S. D. M. 1997, *ApJ*, 490, 493
 Piran, T., Svirski, G., Krolik, J., Cheng, R. M., & Shiokawa, H. 2015, *ApJ*, 806, 164
 Planck Collaboration, Ade, P. A. R., Aghanim, N., et al. 2016, *A&A*, 594, A13
 Polyachenko, V. L., & Shukhman, I. G. 1981, *Sov. Astron.* 25, 533
 Polyachenko, E. V., Polyachenko, V. L., & Shukhman, I. G. 2008, *MNRAS*, 386, 1966
 Pracy, M. B., Owers, M. S., Couch, W. J., et al. 2012, *MNRAS*, 420, 2232
 Pracy, M. B., Croom, S., Sadler, E., et al. 2013, *MNRAS*, 432, 3131
 Rees, M. J. 1988, *Nature*, 333, 523
 Rodriguez-Gomez, V., Genel, S., Vogelsberger, M., et al. 2015, *MNRAS*, 449, 49
 Saxton, C. J., Perets, H. B., & Baskin, A. 2016, arXiv:1612.08093
 Shankar, F., Weinberg, D. H., & Miralda-Escudé, J. 2009, *ApJ*, 690, 20
 Stone, N., & Loeb, A. 2012, *PRL*, 108, 061302
 Stone, N. C., & Metzger, B. D. 2016, *MNRAS*, 455, 859
 Stone, N. C., & van Velzen, S. 2016, *ApJL*, 825, L14
 Strubbe, L. E., & Quataert, E. 2009, *MNRAS*, 400, 2070
 Syer, D., & Ulmer, A. 1999, *MNRAS*, 306, 35
 Tadhunter, C., Spence, R., Rose, M., Mullaney, J., & Crowther, P. 2017, *Nature Astronomy*, 1, 0061
 Taffoni, G., Mayer, L., Colpi, M., & Governato, F. 2003, *MNRAS*, 341, 434
 Tremaine, S., Richstone, D. O., Byun, Y.-I., et al. 1994, *AJ*, 107, 634
 van Velzen, S., Farrar, G. R., Gezari, S., et al. 2011, *ApJ*, 741, 73
 van Velzen, S., & Farrar, G. R. 2014, *ApJ*, 792, 53
 van Velzen, S. 2017, arXiv:1707.03458
 Vasiliev, E., & Merritt, D. 2013, *ApJ*, 774, 87
 Vasiliev, E. 2015, *MNRAS*, 446, 3150
 Vasiliev, E. 2017, *submitted*

Ulmer, A. 1999, *ApJ*, 514, 180
 van Velzen, S., Anderson, G. E., Stone, N. C., et al. 2016, *Science*, 351, 62
 Wang, J., & Merritt, D. 2004, *ApJ*, 600, 149
 Wang, L., Spurzem, R., Aarseth, S., et al. 2016, *MNRAS*, 458, 1450
 Wegg, C. 2013, Ph.D. Thesis,
 Wegg, C., & Bode, J. 2011, *ApJL*, 738, L8
 Weissbein, A., & Sari, R. 2017, *MNRAS*, 468, 1760
 Wevers, T., van Velzen, S., Jonker, P. G., et al. 2017, arXiv:1706.08965
 Zauderer, B. A., Berger, E., Soderberg, A. M., et al. 2011, *Nature*, 476, 425

APPENDIX A: LOSS CONE THEORY

Near a SMBH, stars are disrupted when angular momentum diffusion brings them onto radial orbits. Diffusion through energy space contributes to TDE rates at a vastly lower level. The loss cone is the region of phase space where the specific angular momentum obeys $J < J_{LC}$, where $J_{LC}^2 \approx 2GM_* r_i$ is the angular momentum of the loss cone. The reader interested in a thorough introduction to LC physics should consult Cohn & Kulsrud (1978) and Merritt (2013); our goal here is limited to summarizing those results relevant for our calculations in §2 and §3.

We limit ourselves in this appendix to the special case where the stellar density profile obeys $\rho_*(r) = \rho_0(r/r_0)^{-\gamma}$ and $r \ll r_{\text{infl}}$. Inside the radius of influence, the Kepler potential of the SMBH is $\psi = GM_*/r$; here we use the stellar dynamical convention where specific orbital energy ϵ is positive for bound orbits, as is the gravitational potential. The one-dimensional velocity dispersion is

$$\sigma^2 = \frac{GM_*}{r(1+\gamma)}. \quad (\text{A1})$$

Assuming isotropic velocities, the distribution function is given by an Eddington integral:

$$f(\epsilon) = 8^{-1/2} \pi^{-3/2} \frac{\Gamma(\gamma+1)}{\Gamma(\gamma-1/2)} \frac{\rho_0}{\langle m_* \rangle} \left(\frac{GM_*}{r_0} \right)^{-\gamma} \epsilon^{\gamma-3/2}, \quad (\text{A2})$$

where Γ is the standard Gamma function. In §2, we compute the relaxation time t_r , which is defined in terms of a local diffusion coefficient for the parallel velocity component (Merritt 2013)

$$\begin{aligned} \langle (\Delta v_{\parallel})^2 \rangle &= \frac{32\pi^2}{3} G^2 \langle m_*^2 \rangle \ln \Lambda v (F_4(v) + E_1(v)), \\ E_1(v) &= \int_v^{\infty} \frac{v_f}{v} f(v_f) dv_f \\ F_4(v) &= \int_0^v \left(\frac{v_f}{v} \right)^4 f(v_f) dv_f. \end{aligned} \quad (\text{A3})$$

Here we have rewritten Eq. A2 in terms of the local velocity v with the substitution $\epsilon = \psi - v^2/2$. We evaluate the diffusion coefficient at $v = \sqrt{3}\sigma(r)$. In standard galactic nuclei, the use of $\langle (\Delta v_{\parallel})^2 \rangle$ usually gives a reasonable estimate of the energy relaxation time, but formally speaking, energy relaxation is governed by a nonlocal orbit-averaged diffusion coefficient. When $\gamma \geq 2$, energy diffusion becomes strongly nonlocal. We find numerically that using Eq. A3 to compute the normalization of the energy relaxation time t_r gives results off by a factor of a few when applied to the ultrasteep regime of §2.

Deep in the Kepler potential of an SMBH, the orbit-averaged angular momentum diffusion coefficient (which arises

from $\langle(\Delta v_\perp)^2\rangle$, not Eq. A3) can be approximately evaluated in closed form (Stone & Metzger 2016, Appendix A). This is useful when considering the DTD of ultrasteep stellar density cusps, and in §2 we make use of the closed form expression for LC flux,

$$\mathcal{F}(\epsilon) \approx \frac{32\pi}{3\sqrt{2}} G^5 M_\bullet^3 \rho_0^2 \ln \Lambda \left(\frac{GM_\bullet}{r_0} \right)^{-2\gamma} \left(\frac{\gamma(\gamma-1/2)\Gamma(\gamma)}{\Gamma(\gamma+1/2)} \right)^2 \quad (\text{A4})$$

$$\times \frac{3\tilde{Q}_{1/2} - \tilde{Q}_{3/2} + 2\tilde{Q}_0}{\ln(GM_\bullet/(4\epsilon r_i))} e^{2\gamma-11/2}.$$

Here the dimensionless terms

$$\tilde{Q}_0 \approx \frac{5\pi}{8(2\gamma-1)} \quad (\text{A5})$$

$$\tilde{Q}_{1/2} \approx \pi^{1/2} \left(\frac{1811 - 798\gamma + 16\gamma^2}{120} \frac{\Gamma(4-\gamma)}{\Gamma(15/2-\gamma)} \right. \\ \left. + \frac{2\gamma-1}{4(5-\gamma)(4-\gamma)} \frac{\Gamma(\gamma+1/2)}{\Gamma(\gamma+1)} \right) \quad (\text{A6})$$

$$\tilde{Q}_{3/2} \approx \frac{\pi}{40\Gamma(\gamma-3)} \left(\frac{\pi^{1/2}(8\gamma^2 + 118\gamma - 325) \csc(\pi\gamma)}{\Gamma(15/2-\gamma)} \right. \\ \left. - 15 \times \frac{2^{5-2\gamma}(1-2\gamma)^2(2\gamma-7)(2\gamma-5)(2\gamma-3)\Gamma(2\gamma-8)}{\Gamma(\gamma+2)} \right). \quad (\text{A7})$$

Note that the function $\tilde{Q} \equiv 3\tilde{Q}_{1/2} - \tilde{Q}_{3/2} + 2\tilde{Q}_0$ has singularities at all integer and half-integer values of γ . As these are removable singularities, they do not pose a serious challenge for numerical evaluation, but for the convenience of the reader, the following fitting formula is accurate to within 10% for $0.5 \leq \gamma < 2.95$:

$$\tilde{Q} \approx \frac{1.99}{\gamma-1/2} - 0.0657 + 0.597(\gamma-1/2) - 0.192(\gamma-1/2)^2, \quad (\text{A8})$$

where $\tilde{Q} \equiv 3\tilde{Q}_{1/2} - \tilde{Q}_{3/2} + 2\tilde{Q}_0$.

In ultrasteep density cusps, \dot{N} diverges as one integrates $\mathcal{F}(\epsilon)$ to more and more tightly bound orbits; if there is some large value of ϵ' above which the power law flattens, then $\dot{N} \sim \epsilon' \mathcal{F}(\epsilon')$.

APPENDIX B: PRESCRIPTIONS FOR CALCULATION OF SMBHB TDE RATES

Rodríguez-Gomez et al. (2015) use the Illustris simulation to explore the merger rates of galaxies across a range of redshifts and mass ratios. We employ their fitting formula, Eq. 22 in §4, and list in this appendix the relevant ancillary fitting formulas and fitted constants. In particular, $A(z) = A_0(1+z)^\eta$, $\alpha(z) = \alpha_0(1+z)^{\alpha_1}$, $\beta(z) = \beta_0(1+z)^{\beta_1}$, and $\delta(z) = \delta_0(1+z)^{\delta_1}$. $A_0 = 10^{-2.2287} \text{ Gyr}^{-1}$, and the dimensionless fitted constants are $\eta = 2.4644$, $\alpha_0 = 0.2241$, $\alpha_1 = -1.1759$, $\beta_0 = -1.2595$, $\beta_1 = 0.0611$, $\gamma = -0.0477$, $\delta_0 = 0.7668$, and $\delta_1 = -0.4695$.

This formula is used to estimate merger rates between galaxies with total descendant stellar mass \mathcal{M}_\star , and mass ratio Q_\star . However, in early stages of the merger, dark matter is the dominant constituent powering the action of dynamical friction on the infalling satellite. Thus, in order to compute the dynamical friction inspiral time, we need a stellar to halo mass relation (SHMR). We employ the parametrized SHMR of Moster et al. (2013), which was computed using abundance matching:

$$\frac{\mathcal{M}_\star}{M_h} = 2N(z) \left[\left(\frac{M_h}{M_1(z)} \right)^{-B(z)} + \left(\frac{M_h}{M_1(z)} \right)^{C(z)} \right]^{-1}, \quad (\text{B1})$$

where M_h is total halo mass. This formula employs the following

auxiliary fitting functions:

$$\log_{10} M_1(z) = M_{10} + M_{11} \frac{z}{z+1} \quad (\text{B2})$$

$$N(z) = N_{10} + N_{11} \frac{z}{z+1} \quad (\text{B3})$$

$$B(z) = B_{10} + B_{11} \frac{z}{z+1} \quad (\text{B4})$$

$$C(z) = C_{10} + C_{11} \frac{z}{z+1}, \quad (\text{B5})$$

where $M_{10} = 11.590$, $M_{11} = 1.195$, $N_{10} = 0.0351$, $N_{11} = -0.0247$, $B_{10} = 1.376$, $B_{11} = -0.826$, $C_{10} = 0.608$, and $C_{11} = 0.329$.

Likewise, we convert total stellar mass \mathcal{M}_\star into bulge mass $\mathcal{M}_{\text{bulge}}$ by using tabulated estimates for B/T ratios taken from a large sample of SDSS galaxies (van Velzen 2017). These tabulated estimates are binned by total stellar mass, and we linearly interpolate between different bins. The results are qualitatively similar to parallel SDSS analysis in Kim et al. (2016). The precise tabulated data (van Velzen, private communication) is shown in Table B1. This conversion is necessary to use the $\mathcal{M}_\bullet - \mathcal{M}_{\text{bulge}}$ relation in our estimates of SMBH mass (Eq. 23).

Given the progenitor masses, we now follow the formalism of Taffoni et al. (2003) to estimate T_{DF} , the dynamical friction inspiral time that sets the delay between time of merger and the onset of the TDE rate enhancement. We approximate the dark matter halos of the two progenitor galaxies as NFW profiles (Navarro et al. 1997) with mass density

$$\rho_{\text{NFW}}(r) = \frac{M_h}{4\pi R_h^3} \frac{\delta_c}{c_h x (1+c_h x)^2}. \quad (\text{B6})$$

Here $x = r/R_h$ is a dimensionless radius, c_h is the dimensionless halo concentration parameter and

$$\delta_c = \frac{c_h^3}{\ln(1+c_h) - c_h/(1+c_h)}. \quad (\text{B7})$$

The circular speed $V_c^2(r) = GM(r)/r$ can be computed from the mass enclosed at radius r ,

$$M(r) = M_h \frac{\ln(1+c_h x) - c_h x/(1+c_h x)}{\ln(1+c_h) - c_h/(1+c_h)}. \quad (\text{B8})$$

For a halo of given mass M_h , we define the virial radius as

$$R_h = \left(\frac{3M_h}{4\pi \times 200\bar{\rho}} \right)^{1/3}, \quad (\text{B9})$$

where $\bar{\rho}(z)$ is the Universe's average density at redshift z . We estimate the concentration parameters of the NFW halos using empirical results from weak lensing (Mandelbaum et al. 2008):

$$c = (5.6 \pm 0.9)(1+z)^{-1} \left(\frac{M_h}{10^{14} M_\odot} \right)^{-0.13 \pm 0.07}. \quad (\text{B10})$$

Now we can estimate the dynamical friction inspiral time T_{DF} of a satellite with initial orbital energy E and angular momentum J using Eq. 24. Defining the ratio of halo masses to be $Q_h = M_s/M_h$, we can define the dimensionless constant A from Eq. 24 in two different regimes. When $Q > 0.1$, the satellite galaxy does not lose significant mass from tidal stripping during its dynamical friction-driven inspiral, and the ‘‘rigid body’’ dynamical friction time can be computed with

$$A_{\text{rigid}} = 0.6 f(c_h) \epsilon^\alpha x_c^{1.97} / \ln \Lambda. \quad (\text{B11})$$

Here the Coulomb logarithm $\ln \Lambda = \ln(1 + Q_h^{-1})$, $x_c = r_c(E)/R_h$, $r_c(E)$ is the initial circular orbit radius, the circularity parameter $\epsilon = J/J_c(E)$, and the circular orbit angular momentum $J_c(E) =$

Table B1. Average bulge to total (B/T) corrections for different bins of total stellar mass \mathcal{M}_\star in the van Velzen (2017) sample of SDSS galaxies.

$\log_{10}(\mathcal{M}_\star/M_\odot)$	B/T
8.225	0.0944
8.614	0.1202
8.985	0.1205
9.363	0.1424
9.785	0.2777
10.13	0.4527
10.49	0.5637
10.83	0.6692
11.17	0.7685

$r_c(E)V_c(r_c(E))$. We also define the following dimensionless support functions:

$$f(c) = 1.6765 + 0.0446c \quad (\text{B12})$$

$$\alpha(x_c, Q_h) = 0.475 \left(1 - \tanh(10.3Q_h^{0.33} - 7.5x_c) \right). \quad (\text{B13})$$

However, when $Q_h < 0.1$, the satellite galaxy undergoes significant tidal stripping, increasing the inspiral time substantially. A fitting formula for the inspiral time in this “live satellite” regime, valid for $Q_h < 0.08$, is

$$A_{\text{live}} = \left[0.25 \left(\frac{c_h}{c_s} \right)^6 - 0.07 \frac{c_s}{c_h} + 1.123 \right] \left[B(x_c)Q_h^{0.12} + C(x_c)Q_h^2 \right] \\ \times [0.4 + D(x_c, Q_h)(\epsilon - 0.2)]. \quad (\text{B14})$$

The above formula has been well tested against N-body integrations for $\epsilon \geq 0.3$, and may be unreliable for more radial orbits. It uses the following dimensionless support functions:

$$B(x) = -0.050 + 0.335x + 0.328x^2 \quad (\text{B15})$$

$$C(x) = 2.151 - 14.17x + 27.383x^2 \quad (\text{B16})$$

$$D(x, Q_h) = 0.9 + 10^8(12.84 + 3.04x - 23.4x^2) \quad (\text{B17})$$

$$\times \left(Q_h - \frac{0.0077}{1 - 1.08x} - 0.0362 \right)^6$$

Following the suggestion of Taffoni et al. (2003), when $0.06 \leq Q_h \leq 0.1$, we interpolate linearly between these two regimes¹².

Throughout this paper, we employ a Λ CDM cosmology with the most recent Planck calibration of cosmological parameters: $\Omega_\Lambda = 0.687$, $\Omega_M = 0.313$, and $H_0 = 67.48 \text{ km s}^{-1} \text{ Mpc}^{-1}$ (Planck Collaboration et al. 2016).

¹² While Taffoni et al. (2003) suggest a limiting $Q_h = 0.08$, we find that this produces non-monotonic behavior for $T_{\text{DF}}(Q_h)$. We instead pick a limiting $Q_h = 0.06$ to ensure monotonicity.